Operator Impedance During Physical Human-Robot Interaction: Estimation and Validation

by

Matthew Frazer

A thesis
presented to the University of Waterloo
in fulfillment of the
thesis requirement for the degree of
Master of Applied Science
in
Mechanical and Mechantronics Engineering

Waterloo, Ontario, Canada, 2019

Author's Declaration

This thesis consists of material all of which I authored or co-authored: see Statement of Contributions included in the thesis. This is a true copy of the thesis, including any required final revisions, as accepted by my examiners.

I understand that my thesis may be made electronically available to the public.

Statement of Contributions

Chapter 4, as well as section 1.1.5 of this thesis is based off of a conference paper that was co-authored by myself, Mina Nouredanesh, Dr. Arash Arami, Dr. James Tung, and my supervisor, Dr. Soo Jeon, *Effect of Visual Information on Dominant and Non-dominant Hands During Bimanual Drawing with a Robotic Platform*, presented at the 2019 International Conference on Rehabilitation Robotics in Toronto. Ms. Nouredanesh and I worked together to develop the experimental methodology. Ms. Nouredanesh wrote the code to process the data, while I was responsible for the robotics and implementation of the experiment protocol. The manuscript was cowritten by Ms. Nouredanesh and myself, and contains contributions from Dr. Arami, Dr. Tung, and Dr. Jeon. Sections 4.1 and 4.2.1, along with figures 4.2-4.6 are taken directly from the publication.

Abstract

As the frequency and complexity of physical human-robot interaction (pHRI) increases, so does the need to understand the dynamics of this coupled system in real-time. For haptic displays, which provide information to our senses of touch and proprioception, information regarding the human impedance and intent can drastically improve transparency while maintaining operator safety. Numerous online impedance estimators have been proposed in the literature which make continuous approximations of the coupled dynamics available online, obviating the need for perturbations or cumbersome sensors. However, characterizing and validating the performance of these estimators for pHRI is challenging, since it requires precise knowledge of known, time-varying reference impedances.

This thesis explores the characterization of online impedance estimators using two serial manipulators (known as the BURT system), coupled at their end effectors, to physically simulate pHRI. One acts as the human, displaying a reference impedance relative to a desired trajectory, while the other runs the estimation algorithm and tracks a perturbing trajectory. Several least-squared impedance estimation strategies from the literature are validated on the experimental setup, demonstrating its efficacy and utility. The importance of accounting for the desired human trajectory is highlighted, and future research to apply results from the field of human motor control is proposed.

A bimanual circle-drawing sensorimotor experiment was also conducted with the BURT systsem. Visual feedback on the task performance was withdrawn from one hand at a time and relationships between subject handedness, visual feedback, tracing speed, and circularity were studied. Results show that the non-dominant hand tends to trace less circular trajectories than the dominant hand while both are visible, but inconsistent differences in circularity are present across participants when comparing the performance of each hand in its invisible condition. Both hands showed higher tracing speed when only a single hand was receiving visual feedback, and traced more slowly in the free visual condition.

Acknowledgements

I would like to thank my supervisor, Dr. Soo Jeon, for his insight, patience, and sound advice. I would also like to thank Mina Nouredanesh, Dr. Arash Arami, and Dr. James Tung for their valuable contributions to the motor control research.

Thank you to my partner Julie for her unwavering support.

Dedication

To Annie.

Table of Contents

List of Tables

List of Figures

Chapter 1

Introduction

The modelling and control of rigid robot manipulators is heavily researched and, in general, well understood. There exists a wealth of literature on topics such as controller stability, performance, and efficiency, as well as modelling various classes of manipulators and their system identification. However, models of the robot are only half the picture; the environment with which the robot interacts also influences its performance. A complete system model takes into account both the dynamics of the robot itself and its environment, allowing effective and stable control action to be taken. Unknown, dynamic environments naturally present a particular challenge to sense and thus effectively control the robot within, and perhaps no environment is more unknown and dynamic than human interaction.

Physical Human-Robot Interaction (pHRI) is quickly becoming an important area of robotics research as societal demand for performant, yet safe, robotics grows. Examples of haptic interactions, that is, exchanges of proprioceptive information, with robots that are already quite prevalent include rehabilitation, manufacturing, remote surgery, and many more. Robotic systems designed for rehabilitation could be exoskeletal systems or externally supported, such as the BURT system discussed in detail later in section 2.1. Humans often interact with lift-assisting robots in a manufacturing context, and may guide other robots through their desired motions to teach by demonstration. Of course, the haptic feedback provided during precise teleoperation tasks, such as remote surgery, are integral to successful task performance.

Current control paradigms for these applications contend with challenge of the human environment by taking conservative approaches, such as passive control laws, which may be limited in their performance though they guarantee safety. The virtual stiffness that may be rendered by the teleoperated surgical robot, for example, might be limited by an inflated

safety factor if large variations in the stiffness of the operator must be allowed for. If the robot were able to unobtrusively sense information about the human environment during pHRI, such as operator stiffness, this more complete system model could lead to highly effective haptic interactions that satisfy the requirements safety in presence of spontaneous human action, intuitive interaction dynamics, and unobtrusive sensing.

This thesis concerns itself with estimating the coupled dynamics of the human during pHRI, in an effort to improve both the safety and performance of such tasks.

1.1 Background and Related Works

1.1.1 Haptic Devices/pHRI

Control of haptic devices present a unique challenge because they interact with uncertain environments by their very nature. The "human environment" is often stiff, which is known to cause contact instabilities [57]. Additionally, time delays inherent in the human system are often much larger than in the robotic system, affecting the stability [30], and are not subject to redesign. Work by Gil et. al. [24] suggests that the proportions in which humans add damping and stiffness to a robotic system by interacting with it are such that they often increase the margins of stability. This analysis, however, is not a rigorous proof and does not take into account the time-varying nature of human dynamic parameters. As seen in Vidyasagar [59], a system's time-varying state matrix, $A(t)$, may be Hurwitz for all t but the system may still be unstable.

While there are many examples in the literature of authors deriving stability criterion for specific, simplified haptic systems [17][57][30], Kazerooni [34] took a general approach to investigating how human impedance affects system stability using unstructured dynamic models. He found that system damping, whether physical or virtual, determines the size of the stable region. Limits on system stiffness are in direct conflict with haptic system transparency, defined by Lawrence as the ratio of displayed impedance to desired impedance [37]. Ideally-transparent haptic systems must have zero impedance when emulating free space and be capable of providing an arbitrarily large impedance as the virtual environment (virtual or otherwise) demands it. While this is not physically realizable, an optimal haptic controller would achieve a transparency value as close to unity as possible for the given physical system.

As a simple example, consider a single-DOF haptic interface, perhaps a lever as shown in 1.1. An actuator at the pivot allows some haptic control law to be rendered, perhaps a
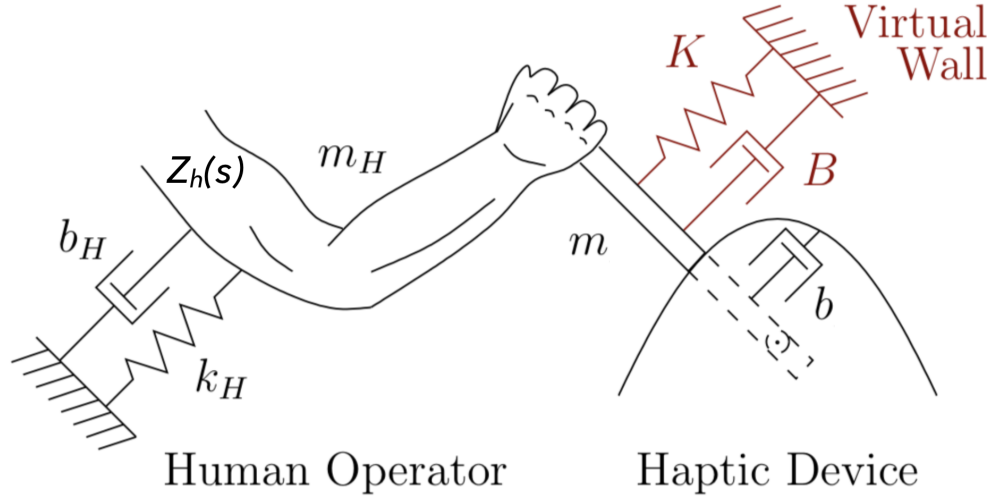
Figure 1.1: A schematic representation of a single-DOF haptic lever and a human operator [30]. The mechanical, virtual, and human systems all contribute to the dynamics of the interaction.

simple virtual spring-damper implemented as a PD controller. The motor and lever have some moment of inertia about the pivot, and the mechanism itself provides some viscous damping. As the controller is implemented on a discrete time controller, with sample time T, the system is passive when [12]:

$$b > \frac{KT}{2} + B \tag{1.1}$$

To guarantee passivity, it is clear that the stiffness the system can provide, and thus its transparency when rendering certain environments, must be limited. Should the safety demands be weakened such that only stability, and not passivity, be asked of the system, then the acceptable values of K increase. Though the stability relationship between virtual stiffness is not trivial[24], for small values of B the stability condition may be approximated by:

$$b + B > \frac{KT}{2} \tag{1.2}$$

When plotted together for a given b and T (see 1.2), the stability regions clearly show what is already fairly intuitive: passivity conditions guarantee safety at the cost of performance. If "stable" is sufficiently safe for a certain application, performance could be
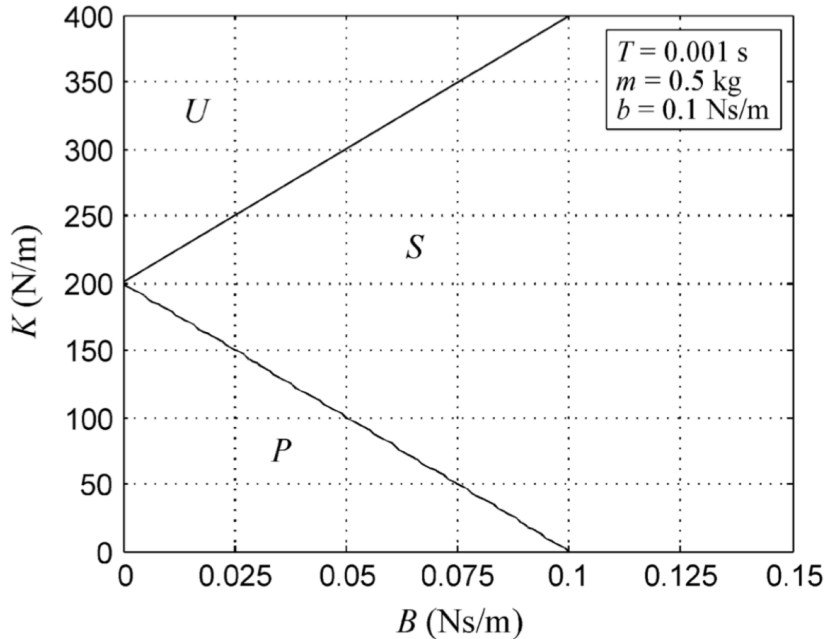
Figure 1.2: The unstable (U), stable (S), and passive (P) regions of the haptic interface as functions of virtual stiffness (K) and damping (B). [24]

maximized by estimating the interaction dynamics and remaining as close as desired to the stability threshold.

1.1.2 Impedance Control and Admittance Control for pHRI

Impedance control, first proposed by Hogan [29], is an extremely popular paradigm for robot interaction control. This genre of controller is appealing for pHRI because it allows the dynamics of manipulator to be regulated, not just its position or force. By analogy to electrical engineering, and impedance is the ratio of voltage, an effort variable, to current, a flow variable. The mechanical equivalent of these, from a system modelling perspective, are force and velocity, respectively. Thus, an impedance controller commands a force output for a given velocity (or position) state. Its dual, the admittance controller, maps velocity outputs onto measured force inputs [44]. Impedance controllers typically excel at rendering low-inertia, low-stiffness environments, whereas admittance controllers struggle with low-inertia, but can render high-stiffness environments well [3]. Citing Adams and Hannaford

[3], Keemink et. al. [36] note the advantage of using admittance control on higher-mass robotic platforms since the "parasitic inertia" of the underlying system can pollute feeling of haptics rendered by impedance control and can be difficult to mask in a stable manner. A formal description of these controllers can be found in section 2.2

The stability of impedance and admittance controllers has been thoroughly studied [9] [14] [10]. Depending on the virtual dynamics they render, admittance controllers may be passive [11]. Presenting dynamics with a virtual inertia of less than half the physical inertia of the device, however, is a sufficient condition for the controller to no longer be passive (though it might be stable) [18]. Generally, decreasing the virtual inertia of the controller makes the interaction subject to instability in contact with increasingly compliant environments [36]. The design of the admittance controller's inner-loop (velocity controller) bandwidth is also critical to maximize the range of stable impedance, though this is balanced by the need for accurate impedance tracking, since it is these inner-loop dynamics which are presented after a large disturbance [20].

1.1.3 Physiology of Human Impedance

The stiffness of a muscle is a nonlinear function of its length and generated force [32]. The force generated by a skeletal muscle for a given level of voluntary contractile effort (VCE) and fatigue is often modeled as a function of both its length and change of length (velocity). The resulting surface is known as a Hill surface, named for physiologist Archibald Hill, and is monotonically decreasing in velocity [38]. That is, muscles are strongest in isometric contraction. So-called "intrinsic" stiffness, as well as contractile force from both reflex and voluntary effort, contribute to the observed stiffness from a muscle [35][51]. The passive, material properties of the tissue, its intrinsic stiffness, instantly produce a force in response to a displacement. On the order of 10ms after an involuntary change of muscle length, reflex action can be observed attempting to correct the change. Voluntary action in response to a proprioceptive stimulus can be an order of magnitude slower than that and is naturally less predictable. Ultimately, a higher generated force will produce a higher stiffness [23].

Skeletal muscles effect motion by creating moments around joints. Since they can only create tension, they are often found in opposing, or antagonist, pairs. In human joint space, increased stiffness about a joint, the change in torque for a given angular displacement, tends to increase with the simultaneous contraction of antagonist pairs [28]. This is known as co-contraction. Notice that this increase in stiffness can happen without a change in net torque on the joint, so the impedance of each joint, and thus the hand, may be controlled independently of the net torque and joint angle. Many authors have created useful models

of muscular neuromechanics which can capture some of the nonlinear interactions between muscle length, velocity, effort, and force [26][25][61].

1.1.4 Human/environment impedance estimation

Much work has been done in the way of estimating various dynamic environmental parameters presented to a robot, including those of a human during pHRI. It is uncommon to find online estimations of environment mass, since this typically involves numerical double differentiation of the manipulator's encoder data, or damping [60]. Most commonly, models of the environment focus on stiffness estimates, rather than the full set of second-order linear model parameters (m, b, and k). In instances of pHRI, stiffness estimation is often favored because it has such a large variance: human joint stiffness can vary by orders of magnitude as a function of voluntary co-contraction [27]. High human stiffness, a natural reaction to unstable conditions [5], is often cited as exacerbating instabilities [23]. Additionally, the inertia of the coupled human system is less important compared to lower-order terms at the relatively low-frequencies common in pHRI [46]. Ultimately, stiffness has the largest impact on the stability of the interaction [14]. The measurements of position and interaction force that can be used to make stiffness estimates can also be used to interpret human intent, such as Duchaine and Gosselin's strategy in [17][16]. Here, online estimates of human stiffness, obtained with a windowed least-squares approach, inform a "stability observer" tasked with modulating virtual damping in response to the changing human dynamics. Concurrently, the robot admittance was tuned according the inferred acceleration intent. The goal of this control scheme was to increase the efficacy of the pHRI by ensuring the robot admittance complimented the human intent while ensuring the coupled dynamics always fell within the margins of stability.

In a similar vein, research has been done using electromyography (EMG) data to make online stiffness estimates during pHRI. Notably, Gallagher et. al. [23] designed an estimator which classified a user's current co-contractive effort into "high stiffness" or "low stiffness" categories. This informed a variable impedance controller in an effort to improve task performance with a haptic manipulator. Further work addressed the stochasticity of the human behavior to reduce chatter [22], but due to sensor noise no refinement to the binning or numerical estimation of stiffness was effective. Recent work by Chen et. al. [8] uses both kinematic and EMG data from sensors on the user to maintain a real-time model of user stiffness. The obvious disadvantage of EMG-based stiffness estimation is the reliance on sensors external to the robot and the calibration required, since all EMG data is interpreted relative to a given user's baseline and maximum voluntary contraction (MVC).

While online stiffness estimates alone can increase haptic task performance and allow for basic real-time models of human dynamics, knowledge of the full characteristics are important for robust control. In both [46] and [8], the researchers make approximations of human damping as a simple function of estimated human stiffness with some success. Complete estimates of human or environment impedance are made by Love in [39] and [40] using a recursive least squares approach. A similar approach is take in [60], but an emphasis is placed on a rapid convergence time for the estimate. Section 3.1 explores least-squared based estimators such as [16], [39], and [60] with more rigor.

1.1.5 Bimanual Circle Tracing

Bimanual circle tracing (BCT) tasks are a canonical human motor control experiment used to explore the sensorimotor patterns and symmetries present (or absent) in both healthy and impaired populations. In BCT experiments, participants are asked to trace circular trajectories, often in the transverse plane, with both hands simultaneously. These circles may be in the same or in opposite directions known as non-mirror symmetric (NMS) and mirror symmetric (MS) tracing, respectively. For example, an experiment by Marteniuk et. al. [41] showed that participants' trajectories were highly likely to converge in phase and amplitude while performing a MS-BCT, leading to a discussion of the role of interhemispheric coupling reducing the independence of each hand during the task. Some evidence shows that MS tasks tend to be more stable, in a neuromechanical sense, than NMS tasks due to the tendency of one hand to spontaneously reverse direction during high-rate NMS motions and settle into an in-phase MS trajectory. [7][4]. Byblow et. al. [6] documented many instances of "spontaneous pattern shifting," where participants would suddenly reverse the direction of one hand (usually their non-dominant hand (NDH)) away from NMS trajectories to the more stable MS paths during a fast paced BCT. This same experiment also found that the circularity performance of the NDH was worse than that of the dominant hand (DH).

BCT experiments lend themselves well to investigations of upper-extremity lateralization, such as handedness, as well as other motor control asymmetries, such as stroke and cerebral palsy (CP). Swinnen et. al [55] considered the effect of different vision conditions on the performance of each hand during a MS-BCT. By blocking visual feedback from the hands, inferences could be made regarding the sensorimotor nature of the BCT in healthy subjects. Similar experiments have been repeated for impaired populations [53]. During the BCT in [13], partially blindfolded (i.e. only one hand visible) and fully blindfolded subjects showed that the absence of visual feedback significantly reduced the reaction times for both arms and led to an increased tracing amplitude in the invisibile arm.

In this study, a NMS-BCT task is performed by subjects on the BURT platform. Visual feedback is withheld from one hand at a time, and the relationship between circularity, tracing speed, and visual conditions are explored. It was hypothesized that the circularity of the NDH would be worse compared to the DH in equivalent visual conditions (that is, the circularity of trajectories traced by the NDH while it is visible would be less circular than those of the DH while it was visible, and similarly for invisible conditions), and that the pace of circle tracing would decrease when both hands are visible, due to the attention split between both hands.

1.2   Contributions and Organization

Given the current state-of-the-art outlined above, the contributions of this thesis is a novel experimental procedure for validating and characterizing the performance of online impedance estimators is demonstrated. This procedure leverages the bimanual nature of the BURT system (see Section 2.1) to create a robot-to-robot interaction in which one manipulator follows human-like trajectories with known, time-varying dynamics while the second manipulator estimates the impedance parameters of first, to which it is rigidly coupled at the end-effector.

Chapter 2 presents the mathematical preliminaries, conventions, and notations used throughout the thesis, including a discussion of the modelling of the BURT system. Chapter 3 considers several numerical online impedance estimation methods from literature and validates their performance using the robot cooperation method briefly described above. Results from a published human sensorimotor control study that leverages the BURT system, along with a discussion of how results from this thesis may enhance future work, are given in Chapter 4.

Chapter 2

Mathematical Preliminaries

2.1 BURT Model

The Barrett Upper-extremities Robotic Trainer, or BURT, is a rehabilitation and pHRI research robot designed by Barrett Technology as an off-the-shelf full 3D haptic device. Each BURT arm has three actuated rotational joints with position feedback from encoders, as well as a passive, unmeasured rotation joint at the end-effector to allow for wrist adduction and abduction. The BURT manipulator may be reconfigured, via quick-release screw mechanism, to the opposite handedness setup by flipping the devie's forearm 180°. The orientation-agnostic design allows two identical BURT units to be used together for bimanual applications, as shown in Fig. 2.1. This section will discuss the kinematic and dynamic models of the BURT as a serial chain manipulator along with the kinematics and initialization of the 6DOF force-torque sensor mounted to the end-effector.

2.1.1 Kinematics

The well-known modified Denavit-Hartenberg (DH) convention can be used to specify coordinate frames along a kinematic chain. For a manipulator with three revolute joints (often denoted by RRR), such as the BURT, it is only required to specify three parameters for each link, i, known as DH parameters: link length, a_i, offset distance, d_i, and twist angle, α_i. The joint angle, q_i, is left as a variable which depends on robot pose. For a complete description of the coordinate frame assignment procedure, see [49]. Due to the symmetry of the BURT system, it is possible to assign identical DH coordinate systems to
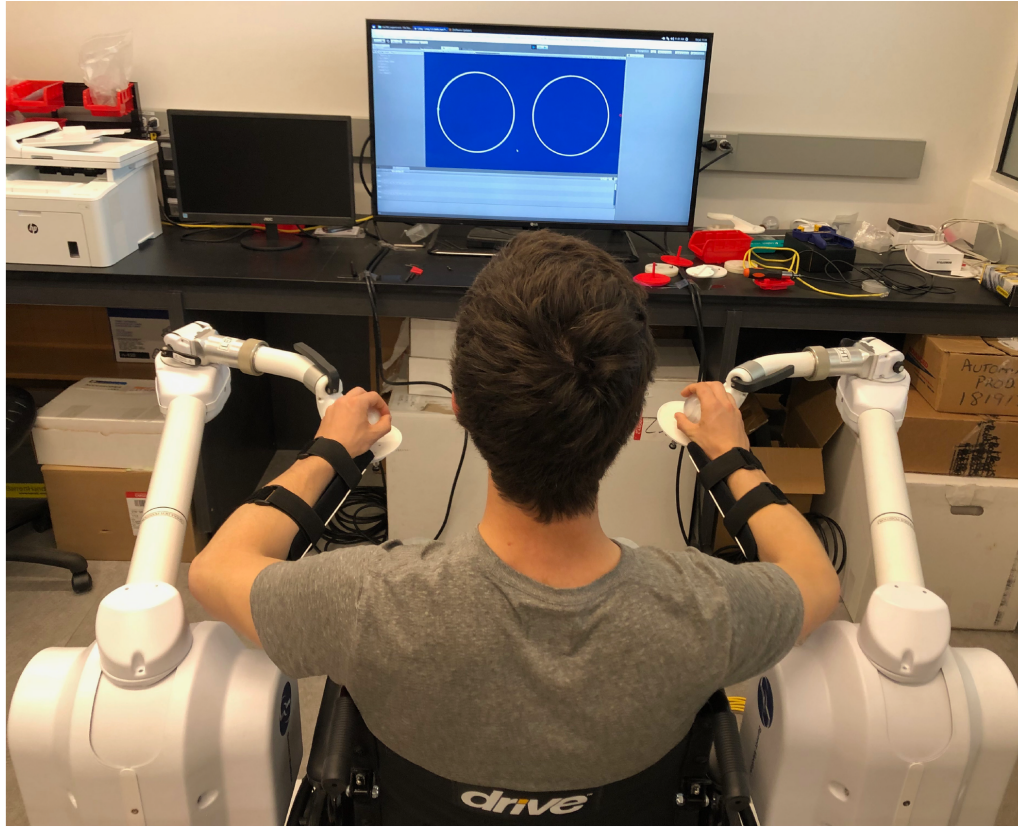
Figure 2.1: A BURT user participating in a bi-manual motor control study

both left and right manipulators, though the distance from the 0th joint to the common origin will be different. Fig. 2.2 shows how coordinate frames may be applied to the manipulator according to DH convention. Note that this pose is not actually attainable given the joint limits of the manipulator in either handedness but serves as a natural configuration for assigning $q = 0$. Positive values of q_i correspond with the right-hand rule about axis z_i.

The particular values for a, d, and α are provided in Table 2.1. Note that the transformation described by the first row describes the rotation from world coordinates to the 0th coordinate frame. The 550mm translation in Y_{WR} shown in Fig. 2.2 is not included in this transformation. With this description of the robot's geometry, the forward kinematics problem may be solved. That is, given a particular manipulator configuration q in joint-space, the position of the end-effector, x, in task-space can be determined. The forward kinematics problem always has a unique solution.
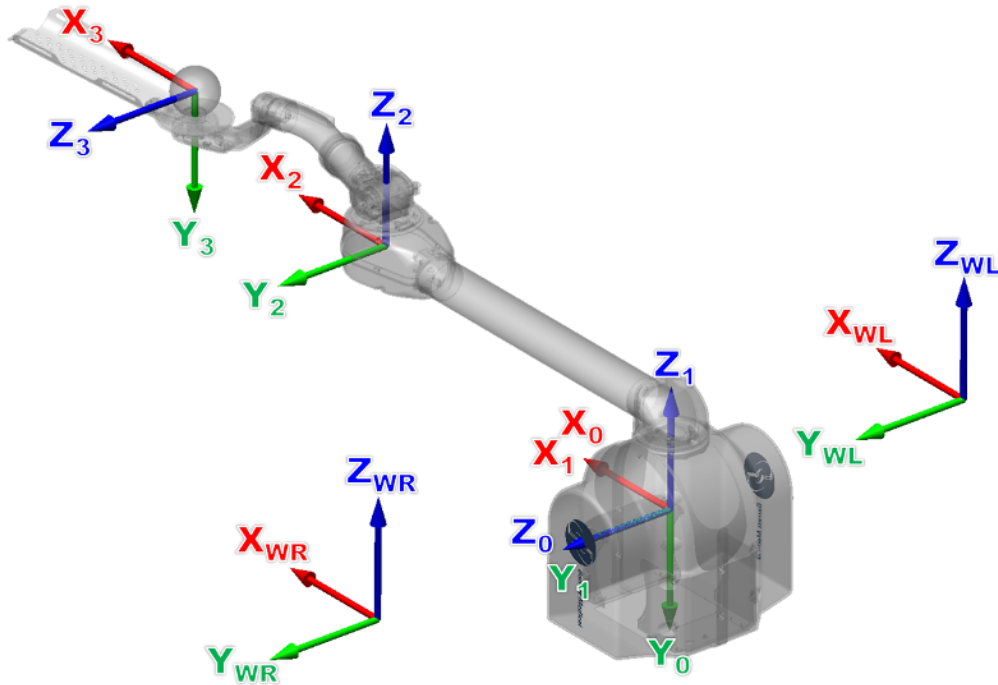
Figure 2.2: The coordinate frames assigned to the BURT system according the modified DH parameters. Depending on the handedness of the arm, the world origin will be located to the left or right, respectively. In this configuration, $\theta_1 = \theta_2 = \theta_3 = 0$ (where θ_i is the rotation of the joint about Z_i). [1]

The opposite problem, to find the joint-space configuration q that achieves a given end-effector position, is known as the inverse kinematics problem. In general, the unique solution is not guaranteed and finding a closed-form analytic solution is not trivial for systems with larger degrees of freedom (DOF), n. For example, Fig. 2.3 shows a simple kinematic ambiguity, in which a planar manipulator may achieve a desired end-effector position with two different joint configurations. For $n > 6$, a robot is said to have redundant DOF, its end-effector may achieve any desired position and orientation in its workspace with infinitely many joint angles. Should x fall outside W, the robot's workspace, no solution to the inverse kinematics problem can be found.

The BURT's joint limits, which for joint 2 depend on the handedness setup of the manipulator, are presented in 2.1. These joint limits eliminate all but one set of solutions to the BURT's inverse kinematics problem. The following equations provide a unique q for

Table 2.1: Table of modified DH parameters and joint limits for the BURT robot.

Link (i)	a_i	α_i	d_i	θ_i	θ_{min}	θ_{max}
		DH Parameters			Joint Limits (rad)	
0	0	$-\pi/2$	0	0	-	-
1	0	$\pi/2$	0	θ_1	-1.01	+0.26
2	0.65	0	0.156	θ_2	-0.96	+0.96
3	0.435	$-\pi/2$	0.069	θ_3	-0.40	+2.84

Figure 2.3: A kinematic ambiguity. It is possible for multiple joint configurations q and q' to postition the end effector at x_d, so a solution to the inverse kinematic problem is not guaranteed to be unique.

any $x = [x_0, x_1, x_2] \in W$:

$$q_1 = \text{atan2}(-x_2, x_0) + \text{atan2}(d, \sqrt{x_0^2 + x_2^2 - d^2}) \tag{2.1}$$

$$q_2 = \text{atan2}(x_1, \sqrt{x_0^2 + x_2^2 - d^2}) - \text{atan2}(a_3 \sin(q_3), a_2 + a_3 cos(q_3)) \tag{2.2}$$

$$q_3 = \text{atan2}(-\sqrt{1 - D^2}, D) \tag{2.3}$$

where d is the sum of offset lengths from the DH table 2.1:

$$d = d_1 + d_2 + d_3 \tag{2.4}$$

and D is the cosine of the angle formed between the second and the third links, found here using the law of cosines:

$$D = (x_0^2 + x_1^2 + x_2^2 - d^2 - a_2^2 - a_3^2)/(2a_2a_3) \tag{2.5}$$

Notice that q_3 must be solved before q_2. Joint-space angular velocities may be mapped to the task-space Cartesian velocity of the endeffector via the Jacobian:

$$\dot{x} = J(q)\dot{q} \tag{2.6}$$

Different Jacobians map joint space onto Cartesian motion at different points, such as the end effector, $J(q)_{eef}$, or the COM of joint i, $J(q)_i$. Notice that $J(q)$, a function of joint positions, is not guaranteed to be invertible, so

$$\dot{q} = J^{-1}(q)\dot{x} \tag{2.7}$$

is only valid for so-called non-singular configurations of the manipulator. The Jacobian also relates joint-space torques to Cartesian forces in task-space at the end effector:

$$F = J(q)\tau \tag{2.8}$$

Due to the the virtual work theorem (see [54]) transpose allows for the transformation in the opposite direction when the manipulator is in static equilibrium:

$$\tau = J^T(q)F \tag{2.9}$$

2.1.2 Dynamics

In the absence of disturbances, the dynamics of an n-DOF rigid robot manipulator may be represented by the following well-known differential equation:

$$D(q)\ddot{q} + C(q, \dot{q})\dot{q} + B\dot{q} + G(q) = \tau \tag{2.10}$$

where $D(q) \in R^{n \times n}$ is the inertia matrix, $C(q, \dot{q}) \in R^{n \times n}$ is the matrix of Coriolis forces, $B \in R^{n \times n}$ is a matrix of viscous friction coefficients, $G(q) \in R^n$ is a vector of gravitational forces, and $\tau \in R^n$ is a vector of motor input torque at each joint.

While the derivation of this dynamic equation is beyond the scope of this thesis, it is worth discussing some of its properties. $D(q)$ is always positive definite and symmetric. $C(q, \dot{q})$ can be defined in terms of the elements of D(q):

$$c_{kj} = \sum_{i=1}^{n} \frac{1}{2} \left\{ \frac{\partial d_{kj}}{\partial q_i} + \frac{\partial d_{ki}}{\partial q_j} + \frac{\partial d_{ij}}{\partial q_k} \right\} \dot{q}_i \qquad (2.11)$$

The gravity vector may be calculated in any pose by :

$$G(q) = -\sum_{i=1}^{n} J(q)_i^T (m_i g) \qquad (2.12)$$

Thus, it is possible to find $D(q)$, $C(q, \dot{q})$, and $G(q)$ with knowledge of the mass, the inertia matrix, and the COM for each link. Viscous friction coefficients $B(q)$ are best determined experimentally for each joint, and its omission from a model can be tolerated from a safety perspective since it is a dissipative force. That is, unmodelled friction present in the system serves only to damp its response by removing energy. Additionally, Colgate and Brown show in [10] that physical damping in the plant allows for a larger range of dynamics to be rendered. Inertial parameters for the BURT system, provided by the manufacturer, allowed for modelling of $D(q)$, $C(q, \dot{q})$, and $G(q)$ without performing a system identification. The mass and COM parameters were verified by comparing simulation and measured values of the steady-state state torque required to counteract the effect of gravity on the robot in several configurations around its workspace. This model can be used for both simulations and computed torque control (see section 2.2).

2.1.3   Force Sensor

In order to sense interaction forces on the manipulator, a 6-DOF force-torque sensor was mounted at the end effector. The sensor, model RFT76-HA01 by Robous Inc., uses capacitive sensors to measure force and torque in three axes each. This adds an additional coordinate frame to the four specified in the previous section, 2.1.1, with the following transformation matrix:

$$T = \begin{bmatrix} 0.866 & -0.5 & 0 & 0 \\ 0 & 0 & -1 & 0 \\ 0.5 & 0.866 & 0 & 0 \\ 0 & 0 & 0 & 1 \end{bmatrix} \qquad (2.13)$$

corresponding to a 90° rotation about the previous frames x-axis, followed by a 30° rotation about its z-axis. The maximum sampling frequency is 1KHz, with an effective resolution of 200mN in each force axis and 8mNm in each torque axis. The sensor is safe for pHRI, since its 300N load capacity in each axis greatly exceed both the 45N Cartesian force limit of the robot and typical pHRI interaction force values from literature.

With the robot in an initial configuration q_0, a reading of the force values from the sensor, F_s, can be decomposed as follows:

$$F_s = F_a + F_g + F_{offset} \tag{2.14}$$

where F_a is the external force applied to the sensor, F_g is the force of gravity due to any mass past the sensor in the kinetic chain, and F_{offset} is a constant offset that is a byproduct of the sensing mechanism. In static operation, a bias force $F_b = F_s$ could be recorded in an unloaded condition (i.e. when $F_a = 0$) and subtracted from all future measurements to remove the DC offset of $F_g + F_{offset}$. However, since the orientation of the sensor changes as a function of q and the robot is not stationary, the original F_g must be added back in to the sensor reading and compensated for in the world frame, rather than the sensor frame. In other words, the measured components of the gravitational force will change as the sensor is rotated, but in the world frame, they are constant.

The procedure to account for this is as follows. F_b is set to F_s when the robot is initialized at q_0 with $F_a = 0$. The known mass of the sensor and end-effector which would contribute to F_{g0} is denoted by m_{eef}. Transformed from the world frame to the sensor frame, the force of gravity that was grouped in with the bias F_{g0}:

$$F_{g0} = R_0^4(q_0)^{-1} \begin{bmatrix} 0 \\ 0 \\ -m_{eef}g \end{bmatrix} \tag{2.15}$$

where R_0^4 is the rotation matrix from coordinates in frame 4 to the world frame (0). To find the true applied force, the bias force is subtracted from the current sensor reading and the initial gravity is added back in. This intermediate vector is then rotated into world coordinates where the constant value of gravitational force on the end-effector is subtracted.

$$F_{a_{world}} = R_0^4(q)(F_s - F_b + F_{g0}) - \begin{bmatrix} 0 \\ 0 \\ -m_{eef}g \end{bmatrix} \tag{2.16}$$
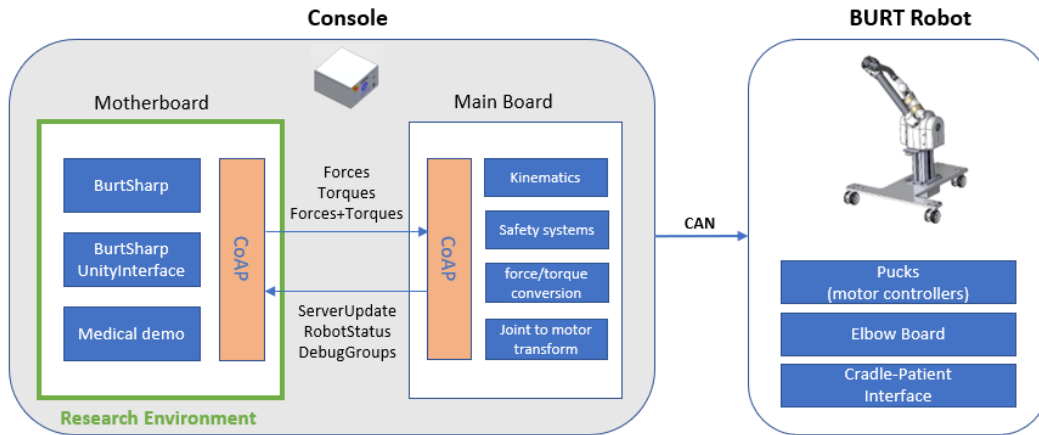
Figure 2.4: A block diagram representation of the BURT's system architecture. [2]

2.1.4   System Architecture

The architecture of the BURT system consists of three subcomponents: the motherboard, a soft-realtime system running the user interface and user-specified control routines; the mainboard, a hard-realtime system responsible for low-level control (e.g. kinematics, gravity compensation, safety systems); and the robot itself, including the Barrett Puck motor drivers which provided closed-loop current control to faithfully actuate the commanded torque. Each of these subcomponents, shown in Fig. 2.4, play an important role in the BURT's performance, but particular attention will be paid to the operation of the soft-realtime motherboard in this section.

The motherboard, which serves as the user interface for the robot, runs the Xubuntu operating system to support control development in C#/Mono with the BurtSharp library. It also allows for tight integration with the Unity game engine with the BurtSharpUnity library, which can be used to facilitate experimental development and quickly create virtual haptic environments. However, since this is not a hard-realtime system, control inputs cannot be sent to the BURT with any guaranteed timing. Additionally, the The hard-realtime mainboard requests control updates from the motherboard at a fixed rate of 500 Hz. The motherboard responds after some delay, determined by competing processes on the Xubuntu, issuing a new control command on average every 2.08 ± 0.26 ms (481 Hz). This rate also determines the maximum data logging rate achievable with the system. The length of the delay between control cycle times is measured by the system and may be retrieved on the subsequent interation of the control loop.

Occasionally, the time between responses from the motherboard may be as large as

16
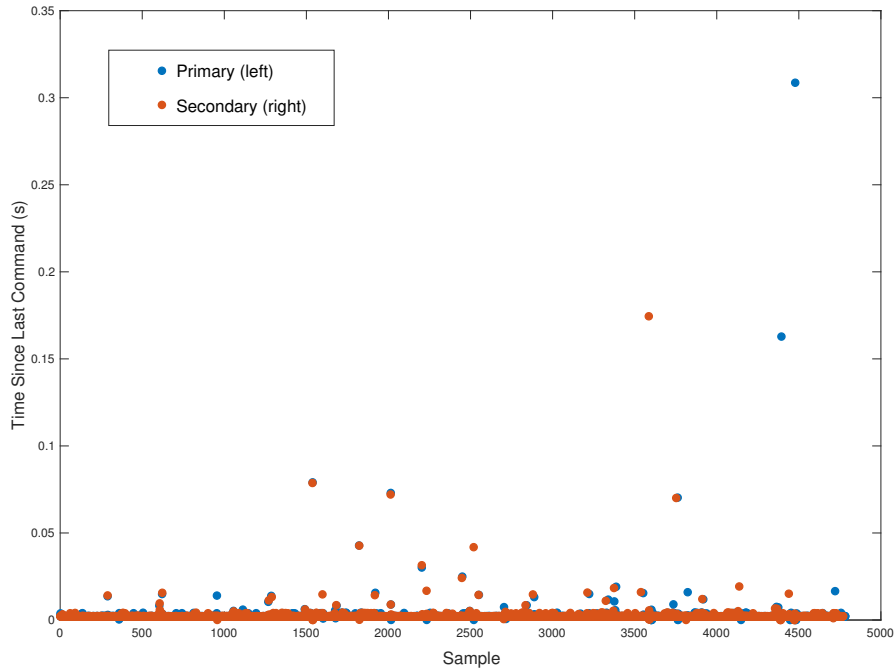
Figure 2.5: Typical delay between control cycle times during a nearly 10 second bimanual experiment using the Unity game engine and a force-torque sensor.

325ms when the motherboard prioritizes other tasks. Figure 2.5 shows a typical concentration of control cycle times for both manipulators in a bimanual experiment using Unity and a force-torque sensor. Instances of control cycle times larger than 50 ms seem to be exacerbated by running the Unity game engine or using multiple force sensors. Investigating the exact nature of these occurrences warrants further investigation.

2.2 Impedance Control for pHRI

Rather than regulating position or tracking a particular trajectory with no constraint on the forces required to achieve it, or rendering a particular force profile regardless of displacement of the end-effector in the case of a force controller, impedance controllers use a desired dynamic model to control the relationship between force (the effort variable) and velocity (the flow variable). This section will discuss implementations of the impedance

17

controller and its dual, the admittance controller.

2.2.1 Impedance Control

Consider a multi-input, multi-output (MIMO) second-order system with following second order dynamics:

$$f = M_d(\ddot{x} - \ddot{x}_d) + B_d(\dot{x} - \dot{x}_d) + K_d(x - x_d) \tag{2.17}$$

where f is the force applied to the system, x is the system position, and x_d, together with its derivatives, form a desired trajectory. Along with system parameters $\{M_d, b_d, k_d\}$, x_d may, in general, be a time varying trajectory, but the dependence on t is omitted for notational simplicity. These dynamics specify a certain relationship between position, time, and force that characterize the system. Thus, if the interaction force during pHRI in a given direction is controlled to satisfy the dynamic relationship in Eq.(2.17), the arbitrary dynamics of the robotic system are effectively masked. Since the desired dynamics are often known in task space, it is common to design for endpoint impedance rather than a individual joint impedances.

A simple example of impedance control is a task-space PD controller, since it provides a control output τ that is a function of a measured position:

$$\tau = J^T(K_v(\dot{x} - \dot{x}_d) + K_p(x - x_d)) \tag{2.18}$$

To better mask the robot dynamics, a computed torque approach may be used if a force sensor is available and the system model is known, or at least well approximated, such as with Eq.(2.10). The computed torque approach, also known as inverse dynamic control, attempts to cancel out the inherent dynamics of the robot using the torque calculated in the model:

$$\tau = D(q)J^{-1}(q)(u - \dot{J}(q,\dot{q})\dot{q}) + C(q,\dot{q})\dot{q} + B\dot{q} + G(q) + f \tag{2.19}$$

Substituting control law (2.19) into Eq.(2.10) reduces to

$$\ddot{x} = u \tag{2.20}$$

By rearranging the impedance Eq.(2.17), the acceleration that conforms to the desired dynamics can be found:

$$u = \ddot{x}_d + M_d^{-1}(f - B_d(\dot{x} - \dot{x}_d) - K_d(x - x_d)) \tag{2.21}$$

If the model has a good agreement with the plant, all non-linear dynamics can be cancelled out and an arbitrary task-space acceleration may be imposed on end-effector. The closed-loop dynamics of the system then become exactly those of Eq.(2.17).
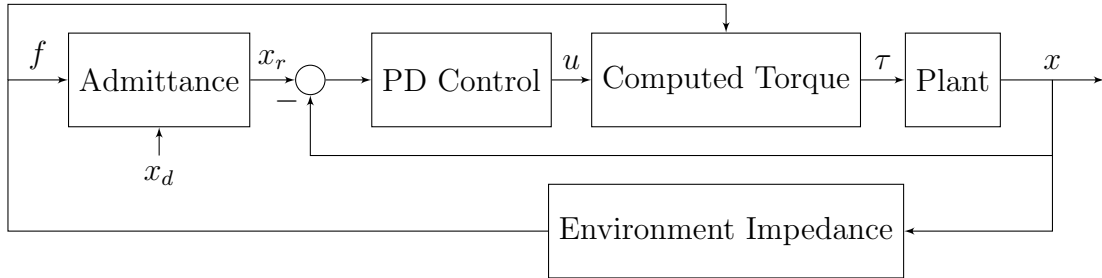
Figure 2.6: Block diagram of a computed-torque admittance controller.

2.2.2 Admittance Control

Admittance control is the dual of impedance control. Rather than measuring the displacement and its derivatives and outputting a force according to Eq.(2.17) as in an impedance control scheme, an admittance controller measures the interaction force and enforces a position output. Since many robots are actuated with torque commands rather than position, an additional inner loop is needed to achieve this position control.

As shown in Fig. 2.6, an admittance controller can be understood as simulating the position response of a system with the desired dynamics Eq.(2.17) in an outer loop and realizing the results of this simulation with a high-bandwidth inner loop position controller. While many options are available for this controller, a high gain, joint-space PD controller with computed torque feed-forward is a performant and relatively simple choice to implement:

$$u = \ddot{x}_r + K_v(\dot{x}_r - \dot{x}) + K_p(x_r - x) \tag{2.22}$$

where K_p and K_v are gains for the PD controller. The reference from the outer loop controller, x_r, is given below. The PD control action u is further substituted into Eq.(2.19) to determine the ultimate control law.

Particular care must be exercised in designing of the inner-loop. It must be sufficiently fast so as not to fall behind the reference signal from the outer-loop, yet must remain stable. A detailed analysis presented by Valency and Zacksenhouse in [58] demonstrates the need for the poles of the inner loop to remain faster than those of the desired dynamics. Frequency content in the trajectory from the outer-loop can excite resonant modes in the inner-loop dynamics and cause instability in the whole system. Ideally, provided the system is linear or at least linearized about an operating point, the PD gains would be selected such that a damping ratio of $\zeta = 0.7$ is a achieved in order to remove any resonance. However, this was not possible in this case because of derivative noise in the velocity signal limiting

the magnitude of K_v and thus the amount of virtual damping available. Consequently, a resonant peak was present in the inner loop's frequency response which is visible in many of the experimental results in Chapter 3.

The outer-loop dynamics may be designed separately in task space based on the desired dynamics for the given task:

$$\ddot{x}_r = \ddot{x}_d + M_d^{-1}(f - B_d(\dot{x}_d - \dot{x}_r) - K_d(x_d - x_r)) \tag{2.23}$$

The reference acceleration $\ddot{x}_r$ may be integrated twice to provide the inner loop controller with the full reference trajectory.

2.2.3   Task-Space Model of Human Arm Impedance

In task-space, the following second order linear model is used to represent the human arm impedance in a given joint configuration:

$$F_h = M_h(\ddot{x} - \ddot{x}_d) + B_h(\dot{x} - \dot{x}_d) + K_h(x - x_d) \tag{2.24}$$

The trajectory x_d is the voluntary path of hand. Parameters M_h, B_h, and K_h do not necessarily represent specific physiological phenomena such as muscle tone or spasticity (often associated with stiffness and damping, respectively), but are rather an abstraction of the local dynamic behavior for given VCE, level of fatigue, etc. As discussed in Section 1.1, the impedance modeled here is the task-space force generated in response to some perturbation and depends on intrinsic material properties of the tissue as well as reflex action. In addition to being physiology-agnostic, this model aligns well with the admittance control laws implemented on many pHRI systems.

As shown in Tsuji et. al [56], it is possible to express the task-space impedance parameters presented in Eq.(2.24) in joint space by using the Jacobian of the kinematic human arm model:

$$K_j = J(q_h)^T K_e J(q_h) \tag{2.25}$$

$$B_j = J(q_h)^T B_e J(q_h) \tag{2.26}$$

$$M_j = J(q_h)^T M_e J(q_h) \tag{2.27}$$

where q_h is the human joint configuration. Thus, if the configuration of the human arm is known, estimates in the task space can reveal the impedance contributions from each joint.

2.3 Parameter Identification

2.3.1 Standard Least-Squares Estimator

Consider the linear system $y = \Phi a$, where y is a vector of measured outputs at n time steps, Φ is an $n \times m$ matrix of m inputs measured at n time steps, and a is a vector of m parameters. Due to the presence of modelling uncertainties and measurement noise, Φa will never match y exactly, so to make this error explicit we instead write:

$$y = \Phi a + \epsilon \tag{2.28}$$

The goal of the least square estimator is to recover the best estimate of the parameter vector a in the presence of the unknown error term ϵ. To quantify the idea of "best", a cost function that minimizes the square of the error can be defined as follows:

$$J = \sum_{i=0}^{n} \epsilon_i = \epsilon^T \epsilon \tag{2.29}$$

To find the minimum, J is expressed in terms of the measurements and differentiated with respect to a. The result is set to 0 and an expression for $\hat{a}$, an estimation of the a, can be found:

$$J = (y - \Phi\hat{a})^T (y - \Phi\hat{a}) \tag{2.30}$$

$$J = y^T y - y^T \Phi\hat{a} - \hat{a}^T \Phi^T y + \hat{a}^T \Phi^T \hat{a}\Phi \tag{2.31}$$

$$\frac{\partial J}{\partial \hat{a}} = -2\Phi^T y + 2\Phi^T \Phi\hat{a} = 0 \tag{2.32}$$

$$\hat{a} = (\Phi^T \Phi)^{-1} \Phi^T y \tag{2.33}$$

The expression $(\Phi^T \Phi)^{-1} \Phi^T$ is also known as the left pseudo-inverse of Φ, or $\Phi^\dagger$. Solving for $\hat{a}$ in this way minimizes the error in the least squared sense over the most recent n samples, but this may present several challenges in practice. First, if a is time-varying, this behavior will not be well-captured in the estimation since standard least squares weights older and newer data equally. Secondly, calculating the pseudo-inverse at each time step involves a matrix inversion that can become intractable even for modest values of n. The inclusion of a "forgetting factor" in a recursive implementation of the least-squares estimator can address these problems.

2.3.2 Recursive Least-Squares with Forgetting Factor

The recursive least-squares (RLS) algorithm is implemented as follows:

$$P[k] = \frac{1}{\lambda}\left(P[k-1] - \frac{P[k-1]\phi[k]\phi[k]^T P[k-1]}{\lambda + \phi[k]^T P[k-1]\phi[k]}\right) \tag{2.34}$$

$$L[k] = \frac{P[k-1]\phi[k]}{\lambda + \phi[k]^T P[k-1]\phi[k]} \tag{2.35}$$

$$\hat{a}[k] = \hat{a}[k-1] + L[k](y[k] - \phi^T \hat{a}[k-1]) \tag{2.36}$$

where $P[k]$ is known as the feedback gain and λ is a forgetting factor. With RLS, it is possible to solve a least squares problem online without recomputing the matrix inverse $(\Phi^T\Phi)^{-1}$. For values of λ less than 1, the estimator weights current data more heavily than older data, allowing the tracking of time-varying parameters. When $\lambda = 1$, all data is equally weighted and the solution is equivalent to that of the standard least-squares estimator considering the entire history of the regressor. As described in [52], in the absence of a sufficiently rich or persistently exciting signal Φ, a constant value for λ could lead to unboundedness in P. Excessively large magnitudes of P makes $\hat{a}$ highly susceptible to noise; modulating $\lambda(\cdot)$ in some manner along with the quality of Φ can be a practical means of avoiding this problem.

As an implementation consideration, the initialization of $P[k]$ should be set to the diagonal matrix $P[0] = p_0 I$ where p_0 is a large positive scalar in order to assure fast convergence. Naturally, reducing the initial error $e[0] = a[0] - \hat{a}[0]$ with a good initial estimate also reduces the convergence time.

Chapter 3

Design of a Novel Testbed for Validating Online Operator Impedance Estimators

This section explores a novel, two-manipulator experimental setup designed to simulate pHRI for the purposes of characterizing and validating online impedance estimators. First, several flavours of least-squared-based approaches to operator impedance estimation from literature are discussed. Next, the motivations and protocol for the experimental setup are described, along with an investigation of admittance controller performance on the BURT. Results of the robot-robot interaction are presented, demonstrating the experiments efficacy and allowing a comparison between estimators from the literature.

3.1   Overview of Estimation Methods

The following online impedance estimation methods solve the linear identification problem of the form: $F_m = \Phi^T \hat{a}$ where Φ is the collection of measured points and $\hat{a}$ contains the parameters to be estimated.

3.1.1   The RLS Approach

In their 1995 paper [39], Love and Book outline a recursive-least-squares method for estimating the impedance of an environment with a discrete-time system. Designed to map

the contact dynamics of the robot's surroundings in order to reduce contact instability, this method is not by itself suitable for general pHRI since it assumes the trajectory of the environment is trivial: $\dot{x}_d = 0$ and $\ddot{x}_d = 0$. Since a human's impedance is often resisting perturbation from a planned, non-trivial trajectory not known *a priori*, more information is required to make a meaningful estimation in some cases. Still, this approach to impedance estimation represents the cornerstone of all RLS-based methods.

Consider a model of the environment similar to 2.2.3:

$$F_m[k] = M_e \ddot{x}[k] + B_e \dot{x}[k] + K_e(x - x_0)[k] \tag{3.1}$$

where $F_m(k)$ is the measured interaction force at discrete time-step k, and x_0 is the initial position of the contact. Using δ to represent a difference with respect to time, the following may be defined:

$$\delta F_m[k] = F_m[k] - F_m[k-1] = \left\{ \begin{array}{c} f_{mx}[k] - f_{mx}[k-1] \\ f_{my}[k] - f_{my}[k-1] \\ f_{mz}[k] - f_{mz}[k-1] \end{array} \right\} \tag{3.2}$$

$$\delta x[k] = x[k] - x[k-1] = \left\{ \begin{array}{c} x_1[k] - x_1[k-1] \\ x_2[k] - x_2[k-1] \\ x_3[k] - x_3[k-1] \end{array} \right\} \tag{3.3}$$

with x_1, x_2, and x_3 corresponding to positions in the x, y, and z-axes, respectively. A discretized model of the environment may then be expressed as:

$$\delta F_m = \left[M_e \left(\frac{2}{T} \right)^2 \left(\frac{1 - z^{-1}}{1 + z^{-1}} \right)^2 + B_e \left(\frac{2}{T} \right) \left(\frac{1 - z^{-1}}{1 + z^{-1}} \right) + K_e \right] \delta x \tag{3.4}$$

where z is the complex variable of the z-transform and T is the sampling time. Rearranging the discretized model yields the following difference equation:

$$\delta F_m[k] + 2\delta F_m[k-1] + \delta F_m[k-2] = [A]\delta x[k] + 2[B]\delta x[k-1] + [C]\delta x[k-2] \tag{3.5}$$

where $[A]$, $[B]$, and $[C]$ are:

$$[A] = \left[M_e \left(\frac{2}{T} \right)^2 + B_e \left(\frac{2}{T} \right) + K_e \right] \tag{3.6}$$

$$[B] = \left[K_e - M_e \left(\frac{2}{T} \right)^2 \right] \tag{3.7}$$

24

$$[C] = \left[M_e \left(\frac{2}{T} \right)^2 - B_e \left(\frac{2}{T} \right) + K_e \right] \tag{3.8}$$

Fitting this into a form that the RLS algorithm may operate on, the output vector y is constructed as:

$$y^T = \delta F_m[k] + 2\delta F_m[k-1] + \delta F_m[k-2] \tag{3.9}$$

while the regressor ϕ is:

$$\phi = \left\{ \begin{array}{c} \delta x[k] \\ \delta x[k-1] \\ \delta x[k-2] \end{array} \right\} \tag{3.10}$$

The parameter matrix $\hat{a}$ is of the form $\hat{a} = [A|B|C]$, and the parameter matrices may be solved for accordingly:

$$\hat{K}_e = \frac{1}{4}[A + B + C] \tag{3.11}$$

$$\hat{B}_e = \frac{T}{4}[A - C] \tag{3.12}$$

$$\hat{M}_e = \frac{1}{4} \left(\frac{T}{2} \right)^2 [A + C - B] \tag{3.13}$$

3.1.2 Time-Varying Forgetting Factors for pHRI

Taking issue with the relatively slow convergence times of simpler RLS-based impedance estimators, a paper by Wang et. al. [60] explored how estimator performance could be improved by better choosing the forgetting factor $\lambda[k]$. While their work specifically mentions estimating human impedance during brief interactions (sub-second convergence times), it does not take into account the human's desired trajectory and thus is restricted to use cases where the operator's path is known.

Two approaches will be described for selecting a time-varying $\lambda[k]$ which take advantage of the saturating property of the arctan($\cdot$) function. First, the method of Diolaiti et. al [15] in which $\lambda[k]$ is inversely proportional to estimation error. Secondly, Wang et. al. proposed a forgetting factor that is related to change of the parameter estimation. That is, as the estimate starts to converge, $\lambda[k]$ increases, while increasing variation in the parameter estimation implies a change in the true parameter value and $\lambda[k]$ is decreased to improve convergence rate.

When the forgetting factor is tied to estimation error, $\hat{e}$, it may be defined as follows:

$$\lambda[k] = 1 - \alpha_1 \left(\frac{1}{\pi} \arctan(\alpha_2(|\hat{e}[k]| - \alpha_3)) + \frac{1}{2} \right) \tag{3.14}$$

where $\hat{e}[k]$ is estimation error: $\hat{e}[k] = y[k] - \Phi[k]\hat{a}[k]$. The control parameters α_1, α_2, and α_3 must be tuned to obtain the desired behaviour of λ. At time-steps with a large $\hat{e}$, λ converges to $1 - \alpha_1$. The rate of this convergence is proportional to α_2 and the size of a "large" error is determined by α_3.

According to the results of Wang et. al., faster convergence is possible by relating $\lambda[k]$ to parameter change. In their scheme, a function $R[k]$ is defined to represent the largest ratio of parameter change between time-steps:

$$R[k] = \begin{cases} \max_{i,j}(\frac{\hat{a}_{ij}[k-l]}{\hat{a}_{ij}[k]}, \frac{\hat{a}_{ij}[k]}{\hat{a}_{ij}[k-l]}), & \hat{a}_{ij}[k-l]\hat{a}_{ij}[k] \neq 0; \\ \infty, & \text{else}. \end{cases} \tag{3.15}$$

where $l \in \mathbb{N}$ is the window length over which the parameter change is examined. This function selects the largest single element change ratio, either gain or loss over the sample window l. If any element is zero, the function should be set arbitrarily large. $R[k]$ informs the calculation of $\lambda[k]$:

$$\lambda[k] = \begin{cases} 1 - \frac{\alpha_3}{\pi} \arctan(|R[k] - 1|), & |R[k] - 1| \geq \alpha_2; \\ \alpha_1 + \frac{1}{\pi}(1 - \alpha_1)(\arctan(1 - |R[k] - 1|)), & \text{else}. \end{cases} \tag{3.16}$$

Tuning parameters $\frac{1}{3} \leq \alpha_1 \leq 1$, $\alpha_2 \geq 0$, and $0 \leq \alpha_3 \leq 2$ define the lower bound of $\lambda[k]$, the threshold of fast changing speed, and the upper bound of $\lambda[k]$, respectively.

3.1.3   Windowed Least-Squares with Offset Matrix

Duchaine and Gosselin took a windowed least squares (WLS) approach to stiffness estimation in their 2009 paper on adaptive impedance control [16]. Though they did not estimate any higher order impedance parameters, citing the dominance of human stiffness at typical pHRI speeds, their estimator did account for "human desired motion" using a linear regression to determine the so-called offset matrix B. For a window length m in n-dimensional space, the pHRI dynamics may be modelled as:

$$F_m = K_e X + B \tag{3.17}$$

where F_m is an $n \times m$ matrix containing the measured forces with rows f_i ($i \in 1..n$), K_h is an $n \times n$ matrix representing the human or environment stiffness, X is an $n \times m$ matrix storing measured positions in task space with rows x_i ($i \in 1..n$), and B is the $n \times m$ offset matrix, whose entries correspond to the force at $X = 0$. The matrix B may be estimated as follows:

$$B = (\bar{f} - V^{-1}\Sigma\bar{x})\mathbf{1}_{[1 \times m]} \tag{3.18}$$

where $\bar{f}$ and $\bar{x}$ are $n \times 1$ column vectors of n row-means from their respective measurement matrix (i.e. $\bar{f}_1 = \text{mean}(f_1)$, $\bar{x}_1 = \text{mean}(x_1)$), V is an $n \times n$ diagonal matrix whose non-zero entries are the variance of each row from X, and Σ is an $n \times n$ diagonal matrix whose non-zero entries are the co-variance of X and F for each dimension:

$$\Sigma_{ij} = \delta_{ij} \text{cov}(x_i, f_j) \tag{3.19}$$

To find human stiffness estimate K_h, windowed least-squares is completed in the usual way, multiplying the offset force measurement by the right pseudo-inverse of X:

$$\hat{K}_e = (F_m - B)X^T(XX^T)^{-1} \tag{3.20}$$

As the authors point out, care must be taken in calculating the pseudo-inverse of X because insufficient excitation in any dimension can lead to a singular or ill-conditioned XX^T. A solution to this implementation challenge is presented in [16] involving selecting only rows for which the position variance is sufficiently large over the window length.

For a three-DOF manipulator and small values of m, taking the pseudo-inverse of X is tractable in realtime on most systems, including the BURT. However, for resource-constrained systems or larger window sizes it may be preferable to calculate a single element of force offset matrix B as described above, subtract it from the measured force, and use the result as $y[k]$ in a RLS scheme. This would also allow for the estimation of higher order impedance terms.

3.2 Design of an Experimental Testbed to Validate Impedance Estimation

Determining the accuracy of an online human impedance estimator is challenging, since it is not possible to measure the true impedance the human presents to the robot during the task without invasive perturbations. Often, impedance estimators are validated by interacting with a machine of known dynamics, such as a damped spring array [50]. The

limitations of this type of validation are obvious; a passive mechanical spring-mass-damper system does not provide a time-varying impedance or a realistically varying set point, both of which are required to meaningfully recreate pHRI. In order to validate the performance of online impedance estimators, an experimental setup has been devised that exploits the bimanual nature of the BURT system. The setup involves the robot-robot-interaction of the left and right manipulators rigidly coupled at their end-effectors. In this configuration, one arm (the leader) takes the place of the robot - tracking a trajectory while running the estimator - while the other (the follower) displays a known, time-varying admittance corresponding to the human. In order for this test be practical, the robot taking the place of the human must: accurately display a realistic time-varying desired admittance within a known tolerance, be moved through a realistic excitation trajectory, and be rigidly coupled to the estimating robot. The following section discusses the design and performance of the impedance controller, the choice of the exciting trajectory, and a description of the robot coupling.

3.2.1 Theory of Operation

The robot-robot interaction described in this chapter is a physical simulation of pHRI in which a pair of BURT arms are rigidly connected (see Fig. 3.1). Admittance control was used in representing the human dynamics because it can fully mask the inertia and lower order dynamics of the manipulator, allowing the system to simulate the effective local mass, damping, and stiffness of the virtual human during the interaction. In its most basic iteration, the testbed models a robot perturbing a human who is attempting to remain stationary (a trivial voluntary trajectory) with a possible time-varying admittance, so the arm representing the human is referred to as the follower. By contrast, the leader applies forces to the follower to move it through a prescribed trajectory. The leader, as the robot in the simulated pHRI, uses the interaction force data it collects along with knowledge of its end-effector position to estimate in real-time the admittance displayed by the follower, ostensibly to improve its controller's performance. While the leader may assume *a priori* that the follower is attempting to remain stationary, this need not be the case. Should the follower be rending its impedance relative to a non-trivial x_d, this may confound the dynamics estimation depending on the sophistication of the estimator.

At its core, the system is a pair of symmetric, rigidly connected manipulators that share a force-torque sensor at their interface. The intent is to demonstrate the utility of such a setup for testing, validating, and characterizing pHRI estimators and controllers in a repeatable testbed with more real-world fidelity than a software simulation.

Figure 3.1: The experimental setup, two rigidly connected BURT manipulators in mirror configuration.

3.2.2   Design and Performance of Experimental Setup

Admittance Control of Follower

The follower robot in this setup is operated based on an admittance controller, meaning it measures the applied force and tracks an output in x according to the desired dynamics. Similar to the controller described in Sections 2.2.1 and 2.2.2, a computed torque admittance controller is used with the omission of the viscous friction term $B\dot{q}$ from Eq.(2.19). Sufficient tracking was achieved without identifying the BURT's B matrix. The desired trajectory for the follower is $\ddot{x}_d = 0$, $\dot{x}_d = 0$, and $x_d = x_0$.

Inner-loop PD gains of $K_v = \mathrm{diag}(8) \in \mathbb{R}^{3\times3}$ and $K_p = \mathrm{diag}(800) \in \mathbb{R}^{3\times3}$ were deter-
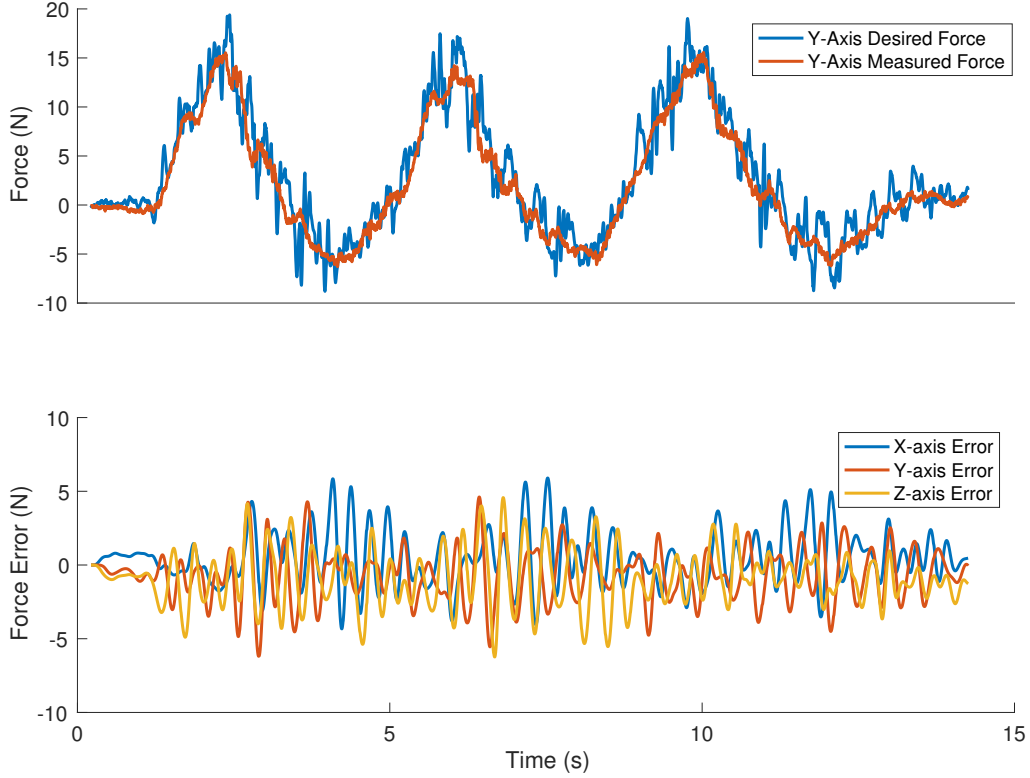
Figure 3.2: Top: Force comparison demonstrating Y-axis admittance tracking. Bottom: Force errors for all three axes.

mined experimentally and provide a balance between admittance tracking accuracy and acceptable stability margins. The under-damped nature of the inner loop controller, a result of the low derivative gain, is a performance limitation discussed in Section 3.3.2, and is necessitated by the phase lag in the BURT's velocity estimate (see discussion of inner loop dynamics in Section 2.2.2).

To characterize the admittance tracking of the follower, consider the force error, σ:

$$\sigma = F_m - (M_d(\ddot{x} - \ddot{x}_d) + B_d(\dot{x} - \dot{x}_d) + K_d(x - x_d)); \tag{3.21}$$

An impedance error of $\sigma = 0$ is achieved when the interaction force matches the force that should have been produced given $x(t)$ and the desired dynamics, which corresponds to perfect admittance tracking. This metric can be calculated for a particular experiment

30
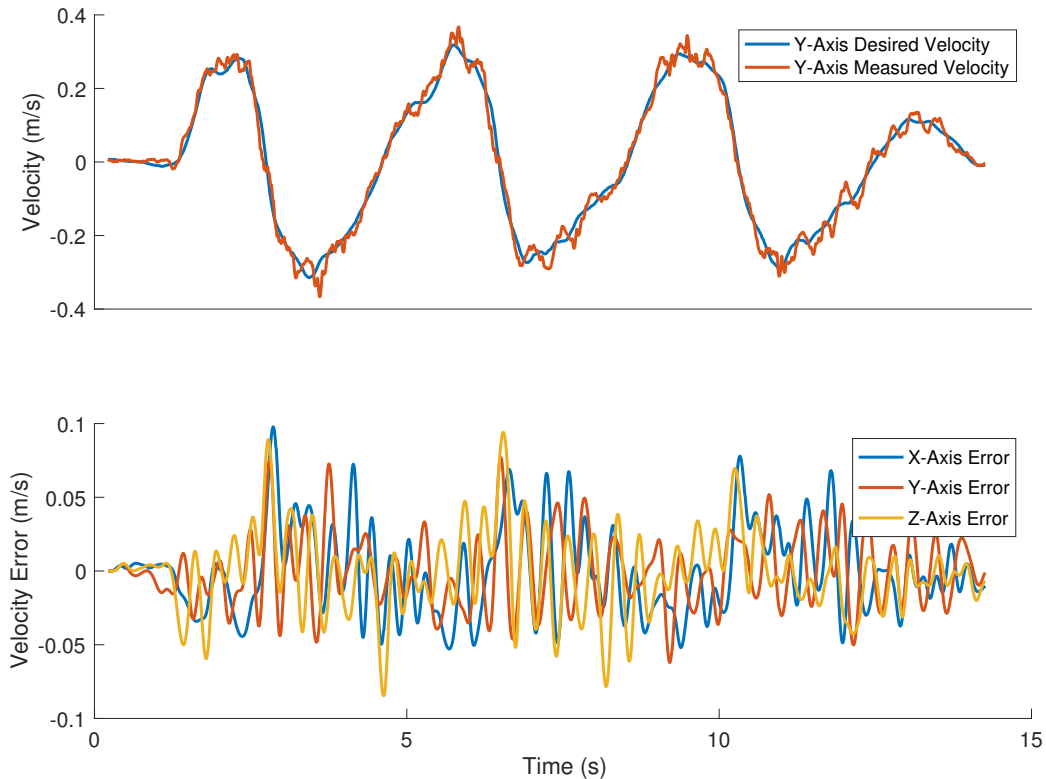
Figure 3.3: Top: Velocity comparison demonstrating Y-axis admittance tracking. Bottom: Velocity errors for all three axes.

offline, given only time-series data of position and force as well as the desired dynamic parameters. However, in practice, determining an accurate $\ddot{x}$ vector from the discrete position data is challenging. Quantization noise is amplified through discrete differentiation, and aggressive low-pass filtering attenuates the signal peaks. The solution proposed in [33] is to apply a Savitzky-Golay filter [48] to the position response, fitting a polynomial of at least second-order to a specified window of position data, and using the second derivative of the fitted curve to approximate the acceleration of the unfiltered measured position data. Since we are only interested in σ as a means of validation after the experiment has completed, this is treated as a smoothing problem and a window may be selected that considers both past and future values of x for a given time.

To make this measurement a human operator physically moves the follower (not yet

coupled to the leader) through an arbitrary trajectory, exciting all three task-space dimensions. Fig. 3.2 shows the results of an admittance tracking characterization. The robot attempts to display a critically damped admittance of $M_d = \text{diag}(5)$ kg, $B_d = \text{diag}(22)$ Ns/m, $K_d = \text{diag}(50)$ N/m while being moved through an approximately elliptical trajectory exciting all three axes.

Equivalently, the endpoint velocity error, $e_{\dot{x}} = \dot{x} - \dot{x}_d$, corresponds to admittance tracking performance (Fig. 3.3).

Sensor noise from the force-torque sensor and derivative noise in the velocity and acceleration measurements contribute to significantly to both sources of error, even after filtering. A large source of error physically present in the interaction are the oscillations due to excitation of the under-damped inner loop controller, as discussed in Section 2.2.2.

Trajectory Design

Clearly, the accuracy of any impedance estimation method depends on the strength and quality of the signal. An excitation that is sufficiently information rich will yield a better estimation than one that contains relatively little. If a strong signal for an abstract parameter identification was desired, any frequency-dense excitation in each axis would suffice. However, since this system is designed to emulate pHRI, the primary constraint on the trajectories is that they are human-like. While it is trivial to generate a frequency-rich trajectory in q that satisfies formal conditions of persistent excitation, it would not serve to meaningfully validate the impedance estimator if the bandwidth of this trajectory was outside what is achievable by a the human arm. Further, an appropriate trajectory must be representative of common motor behaviour to achieve similitude.
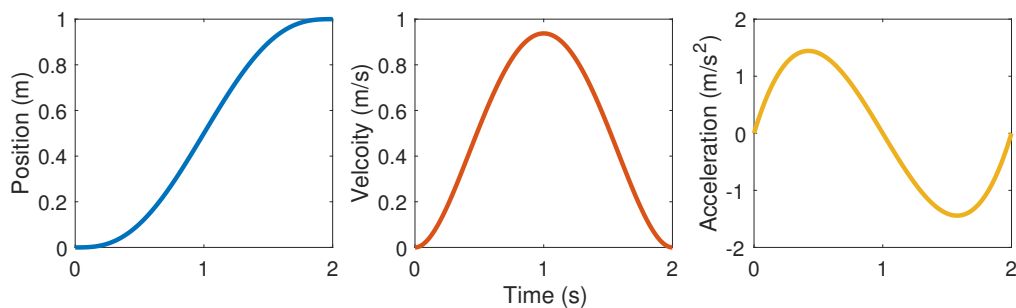
Figure 3.4: Example trajectories that satisfy the Flash-Hogan minimum jerk criteria, $x_0 = 0$, $x_f = 1$, $t_f = 2$.

A natural candidate for an exciting trajectory that respects these constraints is Flash and Hogan's minimum jerk trajectory [19]. They found that for point-to-point upper extremity motions, the velocity profile of the hand follows a distinct fourth-order bell shape which corresponds to the movement that minimizes jerk, the third derivative of position. Specifically, their empirical data shows that in a given direction, a movement from x_0 to x_f over t_f follows:

$$x(t) = x_0 + (x_0 - x_f)(15\tau^4 - 6\tau^5 - 10\tau^3) \qquad (3.22)$$

where $\tau = t/t_f$ represents the fraction of the movement's duration. The trajectory in Eq.(3.22) and its derivatives are shown in Fig. 3.4. They are used in the experimental trials to create a reasonably human-like motion that would likely occur during a typical pHRI.

Description of Coupling

Despite each BURT manipulator lacking a wrist, the symmetry of their kinematics allows robot-robot interaction to occur without the need for a passive wrist joint. In fact, when two BURT arms are configured in opposite handedness and have an overlapping workspace, the XZ-planes of their end-effector's coordinate frame (Fig. 2.2) will be coincident. Rotations about the Y_3 vector are allowed by the built-in passive bearings (Fig. 3.5). To maintain
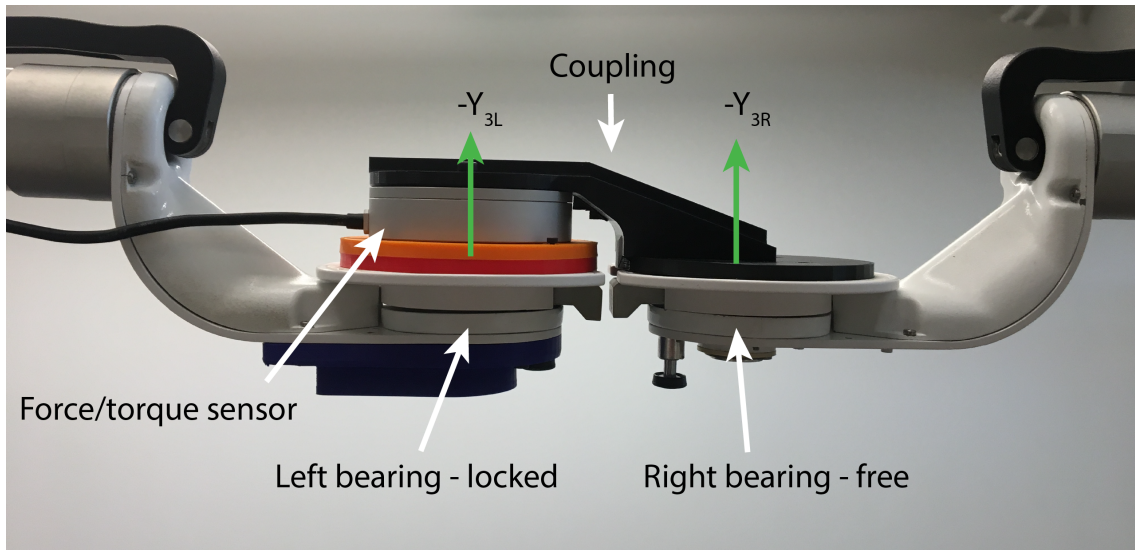
Figure 3.5: A labeled close up of the robot-robot coupling.

the rigid kinematic chain between the left arm and the force/torque sensor, the left bearing must be locked. A torsionally-stiff pin through the centre of the bearing bridges fixturing (red and dark blue parts) that is attached to either side of the rotating surfaces.

Because the end-effectors have volume, they cannot be exactly collocated. Thus, there will always be some misalignment of the platforms. This is compounded by play about the Z_3 vector, visible in the figure as uneven spacing between the top and bottom halves of the bearing. To compensate for this, the coupling is 3D printed with sufficient compliance to absorb the misalignment tolerance – at the expense of a small internal wrench.

3.3   Experimental Trials

The experimental setup was tested with a series of trials designed to test the performance of the three methods outlined in 3.1. In the first trial, the follower displayed a constant impedance to validate the basic RLS algorithm. For the second, step changes in the displayed admittance allowed for comparison between $\lambda[k]$ definitions. Finally, in a third
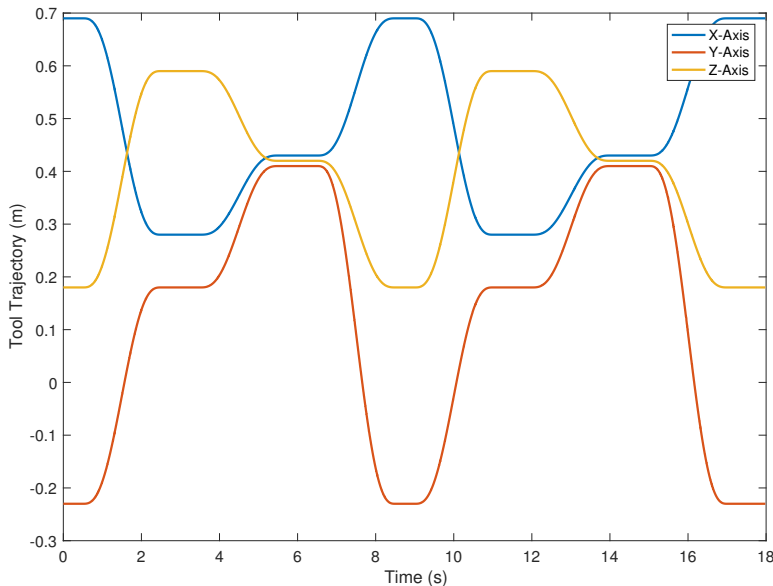
Figure 3.6: The excitation trajectories for a point-to-point test. Each path between targets satisfies a Flash-Hogan minimum-jerk trajectory.
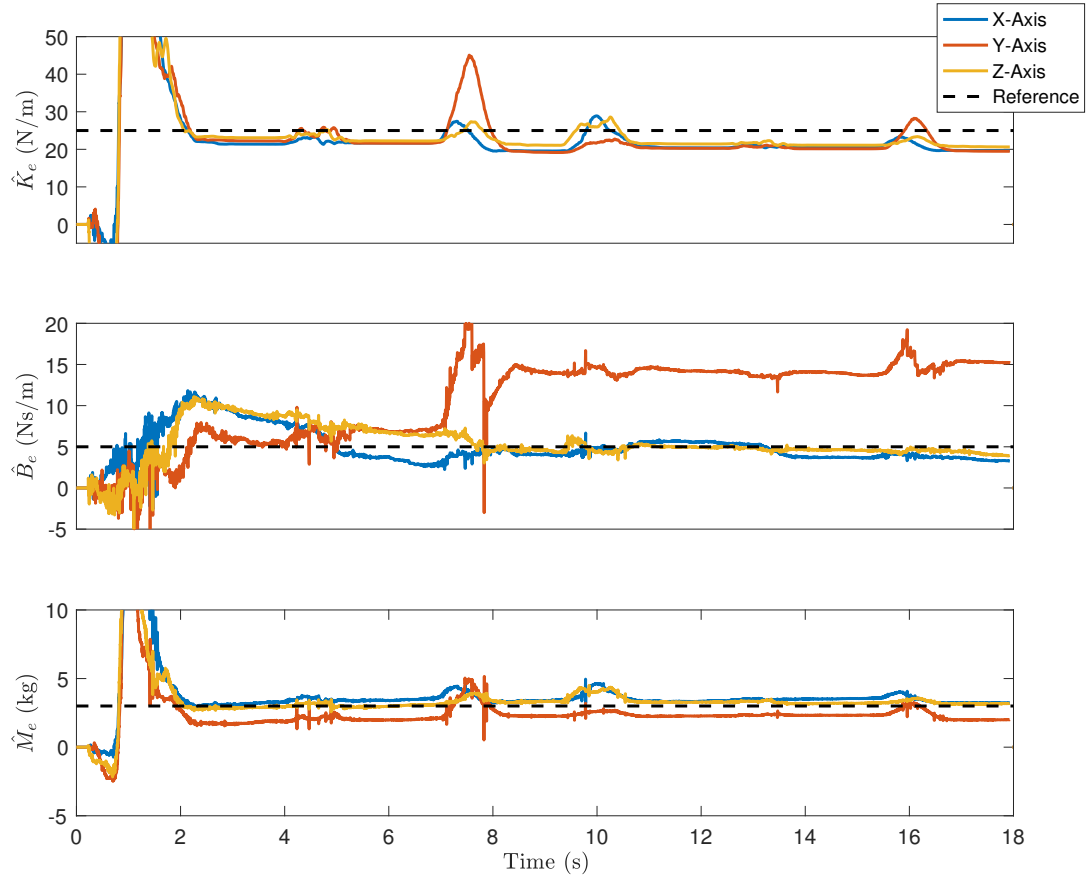
Figure 3.7: A typical result for a constant admittance parameter estimation in three axes using an RLS estimator with constant λ.

trial, the follower tracked a non-zero trajectory while displaying a constant impedance to demonstrate the value of the offset matrix B in WLS method.

3.3.1   Results

Constant Admittance

For these investigations, point-to-point movements were provided as excitation to the follower while it displayed a constant admittance. Fig. 3.6 shows two cycles of the leader's

desired trajectory moving between three target locations in each Cartesian axis. The shape of each section minimizes the jerk when moving from the initial position to final position over a duration of 2 seconds, with a delay of 1 second between targets. In this trial, the desired dynamics of the follower were $M_d = \text{diag}(3)$ kg, $B_d = \text{diag}(5)$ Ns/m, $K_d = \text{diag}(25)$ N/m.

Fig. 3.7 shows a typical RLS estimator with a constant value for forgetting factor $\lambda = 0.999$, as presented in Section 3.1.1, approaching the true parameter values with reasonable accuracy. After a settling time of approximately 1.5 seconds (the leader doesn't excite the follower for the first 0.5 s of the experiment), the mean-absolute-error in (MAE) stiffness estimations are 10%, 11%, and 14% in the x, y, and z-axes, respectively while the MAE in inertia estimations are 8%, 23%, and 16% over the 18-second trial. Convergence performance of the estimator for damping was as slow as 8 seconds.

Tracking in the y-axis was notably poor here, settling near 15 Ns/m after an unknown disturbance along its travel around 7 seconds into the trial. After converging, the MAE in damping was 6%, 185%, and 11% in the in the x, y, and z-axes, respectively. These results are typical for the estimation of the damping parameter, which was observed to be consistently the slowest to converge and most sensitive to numerical disturbances. These results set a baseline for understanding the performance of the testbed under straightforward conditions where the estimation is not complicated by variations in impedance or by a non-zero trajectory in the follower. The effects of measurement noise, variable sampling frequency, and the bandwidth of the exciting trajectory are present, making these trials a useful characterization of the system.

Variable Admittance

In variable admittance trials, the leader moves through similar minimum-jerk trajectories as the constant admittance trials while the follower switches the desired dynamics it renders at each target location. This allows for comparison of convergence times between time-varying forgetting factor methods. Fig. 3.8 shows a typical example of convergence after a step change in displayed inertia from $M_d = 3$ to $M_d = 8$ kg for both error-based and parameter-change-based definitions of $\lambda[k]$.

The error-based $\lambda[k]$ is calculated using tuning parameters $\alpha_1 = 0.002$, $\alpha_2 = 100$, and $\alpha_3 = 0.01$. These parameters were obtained after extensive trial and error experimentation and provided a favorable balance between convergence time and over-sensitivity to measurement noise. For the parameter-based definition of $\lambda[k]$, the tuning parameters were chosen as $\alpha_1 = 0.99$, $\alpha_2 = 5$, and $\alpha_3 = 0$. Again, these were determined experimentally, as

36
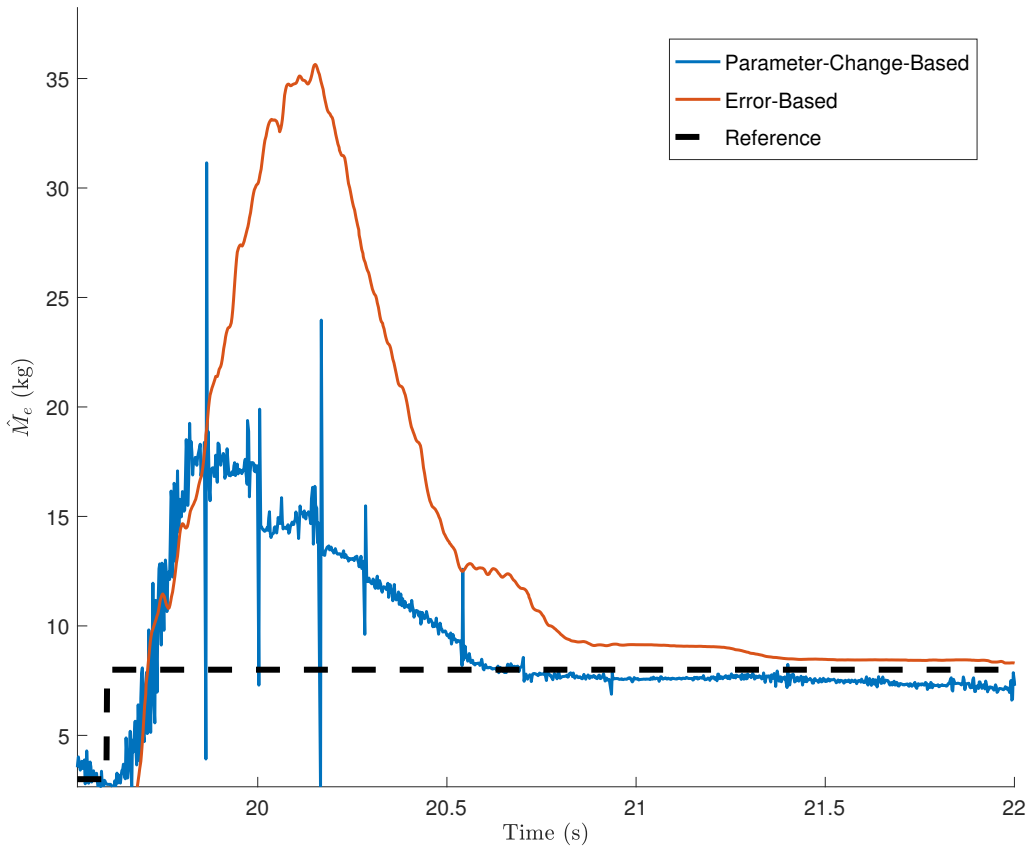
Figure 3.8: The parameter-change-based definition of $\lambda[k]$ (blue) tends to shorten convergence time to the true value (dashed black) after a parameter step change compared to the error-based definition (red).

Wang et. al. concede in [60] (where they provide a qualitative explanation of tuning proce-dure) that these parameters must be "... hand-crafted for the proposed method, as for any similar methods of variable forgetting factors." While variation in the α-parameters for each method would, of course, change the results presented here, their values were selected so as to allow fast convergence time with low steady-state error.

When $\lambda[k]$ was defined according to the error-based method, it settled to 20% of the desired value within 1.2 s. Once settled, it had an MAE of 15%. The parameter-change-based method converged more quickly by 0.3 s with a smaller overshoot, supporting the
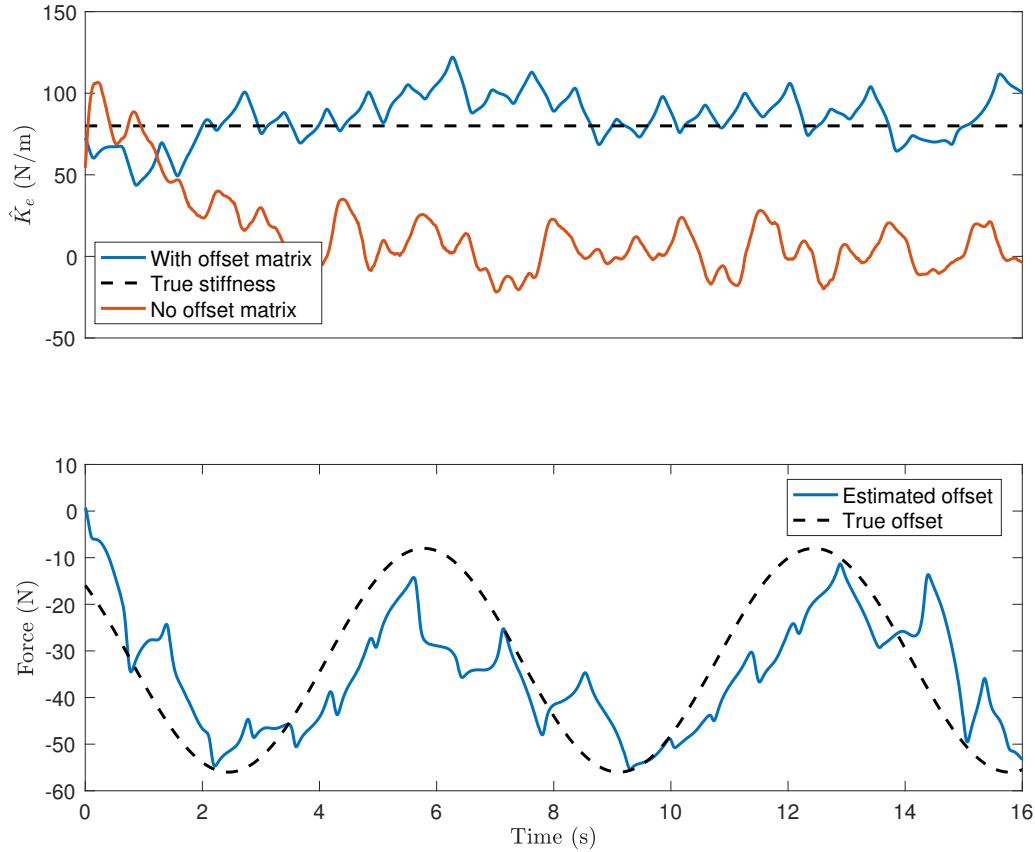
Figure 3.9: Results from a trial with a non-zero follower trajectory in the y-axis. Top: Stiffness estimates using the WLS method, which include an offset matrix, compared to an RLS method without, while the follower traces a sinusoidal trajectory. Bottom: The true value of the force offset compared to the estimated, B.

benefits described in the literature. Additionally, the MAE was only 9%. However, the peak-to-peak noise on the parameter-change-based signal was markedly higher, including several instances where estimations at consecutive timesteps differed by at least 10 kg.

Non-Zero Follower Trajectories

When the follower has a non-constant x_d, akin to the human also moving along some voluntary trajectory, that path must be known (or at least approximated) in order to

38

estimate the admittance parameters. Since this information is not accessible outside the mind of the operator, it might be estimated through statistical inference as in Section 3.1.3. In a trial that demonstrates this, the leader drags the follower through an ellipse in $\mathbb{R}^3$, the follower's position error is measured relative to a setpoint x_d that is translating in the positive y-axis. The changing x_d means the location of the coupling relative to the initial position is no longer exactly proportional to the force produced by the desired stiffness component of the admittance, so the previous methods fail to estimate the stiffness accurately (Fig. 3.9-top).

The offset matrix calculated in 3.18 compensates for the changing set-point, allowing this method to make a reasonable approximation of the stiffness with limited information (see Fig. 3.9-bottom). A window length of 250 samples was used, which is approximately 0.5 s. Even over a relatively large window, the offset matrix was quite sensitive to noise and a 500-sample trailing moving mean filter was applied. This affects convergence time and, as can be seen from the phase delay in the force offset tracking performance, may present a challenge in regards to pHRI. Section 3.4 proposes future research into an alternative method that avoids the noise inherent in the statistical approach to estimating the B matrix.

Since this method does not take into account higher order dynamics, it tends to over-estimate stiffness. The value of the desired stiffness for this trial was $K_d = \text{diag}(80)$ N/m. The MAE for the stiffness estimate that included the offset matrix is 16%, while the estimate which did not take into account the force offset failed to converge and oscillated around 0.

3.3.2 Discussion

The results presented above corroborate the usefulness of the pHRI testbed proposed in this chapter, while also highlighting some of the challenges. Results from the literature are confirmed; for example, the parameter-change-based definition of $\lambda[k]$ due to Wang et. al. is shown to converge more rapidly with less overshoot after a step change compared to the error-based method on a similar time-scale (0.25s) to the results in their 2009 paper [60] (Fig. 3.8). Additionally, the simulated voluntary human movements that resulted in non-trivial follower trajectories could be approximated by the offset matrix proposed by Duchaine and Gosselin [16] (Fig. 3.9). While the authors of that paper only provided high-level experimental results demonstrating improved task performance as evidence of their stiffness estimator's success, the experimental setup presented here allows for a more detailed examination of human voluntary trajectory approximation in a controlled setting.

However, oscillations from the excitation of under-damped modes of the inner loop controller continue to pollute the impedance rendering and can lead to instabilities of the stiffer coupled system. This limits the safe allowable impedance of the leader robot, in turn preventing accurate trajectory tracking and sufficient excitation in the measurements, ultimately leading to poor estimates saturated with noise. An in-depth study into joint velocity measurement or observation which can produce a higher fidelity signal is recommended, as this would allow for a larger virtual damping gain, eliminating this problem.

The geometry of the end-effector coupling also contributes significantly to estimation error (see Section 3.2.2). Since the end-effectors cannot be truly collocated, rotation about the free bearing by the opposite end-effector leads to a relative translation in the XZ-plane of the end-effector coordinate frame. This slippage, though required for the robot-robot cooperation of two 3-DOF manipulators, is the manifestation of the departure from redundant human kinematics. The relative motion between end-effectors that would ideally be collocated adds position error into the estimation not present in true human-robot interaction.

3.4   Future Work

Identifying human voluntary trajectories in an online impedance estimator is a natural application of results from the field of inverse optimal control. As Flash and Hogan's early work in this area [19] demonstrates, it is possible to have a very accurate prediction of the desired, unperturbed motion given the category of task being performed, i.e. point-to-point reaching. All that is required is a cost function that humans tend to minimize for that task, such as minimizing jerk. If their behaviour matches this criteria, the person can be modelled as an optimal controller, the control input u that is the solution to:

$$\min_{x(\cdot),u(\cdot),T} \int_0^T J(x(t),u(t))dt \tag{3.23}$$

where x is the state of the system, constrained by the system dynamics. J is the running cost function:

$$J(x(t),u(t),\alpha) = \sum_{i=0}^{n-1} \alpha_i j(x(t),u(t)) \tag{3.24}$$

in which α is a vector of n weights for the n sub-components of the cost, $j(x(t),u(t))$. For example, a hypothetical cost function may have $n = 3$ sub-costs related to $\dot{x}$, $\ddot{x}$, and

control effort u. Each of these will have some relative importance α to the final cost and thus some influence on the behaviour (or may not contribute if $\alpha_i = 0$).

Determining the weights of a hypothetical cost function from observed behaviour, for example time-series force and position data, is the process of inverse optimal control (IOC). The numerical methods to achieve this are beyond the scope of this document, but the field is rich with examples of both low-level (core balance [45]) and high-level (path planning [42]) neuro-motor processes that can be well described by a custom-fit cost function. This cost function, then, prescribes a very specific control response given a particular task and serves as a powerful and compact way of quantifying human behaviour (the disadvantage, of course, being the involved empirical data collection for each unique task – there is no universal human cost function).

Once a cost function is known for a particular task, a solution to the optimal control problem may be used to obtain an approximation of the eventual trajectory. In the case of minimum-jerk point-to-point reaching task, this is the fifth-order polynomial $x(\tau, x_0, x_f)$. If an online estimator could identify the constants τ, x_0, and x_f, the hidden human voluntary trajectory would be known. A process to determine these parameters would likely depend on context clues from the task as well as inference of human intent (see Section II of [16]), since the true human voluntary trajectory is perturbed by the presence of the robot's dynamics during pHRI. Ultimately, a robust operator impedance estimator must draw from the field of neuromechanics as much as from the fields of robotics and control.

Chapter 4

Applications of the BURT Platform to Human Sensorimotor Research

The design of future pHRI systems must rely on an understanding of human motor control as much as they do on robot control. Advancing knowledge in neuromechanics will ultimately lead to more effective human-facing robotics by improving intent detection and human modelling, as well as inspiring human-like controllers. Up to this point, this thesis has focused on how a robotic system might better estimate human interaction dynamics. This section will briefly demonstrate how the BURT platform can contribute to human motor control research. Specifically, this section introduces the experimental investigation on how the visual information affects dominant and non-dominant hands during bimanual circle tracing.

Beyond its suitability for pHRI research, the BURT platform constitutes a nearly off-the-shelf system for conducting human motor and sensorimotor control experiments. Owing to its design as a medical rehabilitation device, it is a relatively low impedance interface for capturing and guiding motion of the upper extremities through their natural range of motion, acting as a three DOF manipulandum. Additionally, the BURT platform is easily extensible to bimanual investigations, is tightly integrated with the Unity game engine which can be used as a framework for including graphics and implementing experimental protocols, and incorporates features such as virtual walls and speed limits, to improve the safety of the interaction while reducing experiment development time.

This section will describe a novel sensorimotor control experiment conducted on the BURT in collaboration with M. Nouredanesh [43], discuss future work in this area, and
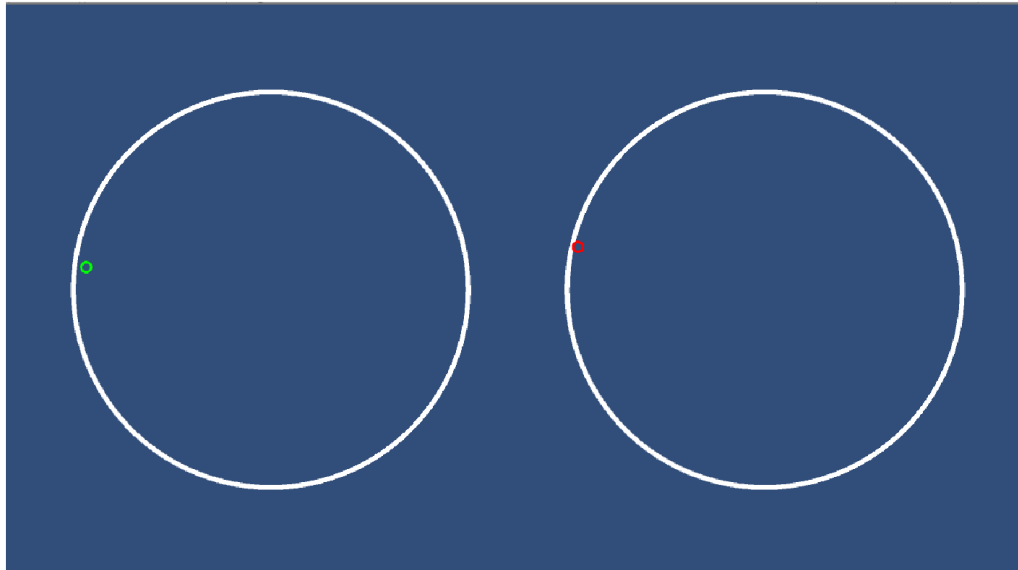
Figure 4.1: A screen-shot of the visual feedback interface for the experiment. The large white circles represent the target trajectories for each hand. The small green and red circles represents the relative locations of the left and right hands, respectively.

suggest possible improvements that could make the platform even better suited to ongoing research.

4.1 Method

4.1.1 Participants

Six healthy, adult participants (5 male, 1 female, aged between 24-35 years), all self-reported as right-handed, with no history of upper-extremity injuries or neurological disorders, were recruited in this experiment. None of the participants had any previous experience with the robotic apparatus or performing bimanual circle-drawing tasks.

4.1.2 Apparatus

Subjects were comfortably seated between the BURT arms. A 43-inch, high-definition, LED display, placed 1.6 m in front of the subject, displays two circles, representing the

desired left-hand and right-hand trajectories (see Fig. 4.1). The user interface is created in the Unity game engine. The displayed circles correspond to two 0.2 m diameter circular trajectories with centers spaced 0.4 m apart in the BURT's workspace. The positions of the subject's left and right hands with respect to the desired trajectories are displayed as green and red markers, respectively. Two distinct trajectories are displayed, rather than mapping the subjects' relative hand locations onto a single circle, to provide an intuitive feedback interface and eliminate the decoding of which marker corresponds to which hand.

While interacting with a BURT arm, subjects grip a molded plastic sphere with a pronated forearm configuration and are coupled to the end-effector using a padded cuff. The BURT tracks the subject's hands' trajectories, while also constraining them to the transverse plane at a height determined to be comfortable by the subject at the outset of the experiment. This provides support for the upper limbs during the trials, minimizing shoulder fatigue.

4.1.3 Protocol

To compensate for the effect of cross-limb training/skill transfer [31], e.g. bilateral access hypothesis, 2 sequences i.e. A-B and B-A, were considered (see Figure 4.2-left panel), where the visual feedback from the left NDH and right DH were withdrawn from sequences A and B, respectively. Participants were instructed to trace the contours of template circles with both hands as quickly and accurately as possible in a non-mirror-symmetric, counter-clockwise mode. A 60-second familiarization step was performed by each subject prior to the experiments. Subjects alternated between 30 s of rest, to further minimize fatigue, and 60 s of continuous circle-drawing in each of four experimental conditions (see Fig. 4.2-left panel). In conditions A_1 and B_1, free-visual conditions (baseline), visual position feedback was provided for both hands. In conditions A_2 and B_2, the visual feedback for the left hand (the green marker) and right hand (red marker), were removed, respectively. In conditions where only one hand's marker is visible, that hand is said to be in its visually-guided mode, while the hand without the marker is said to be in its invisible mode. Signals, i.e. x and y trajectories from both hands, were recorded synchronously with an average sampling rate of $f_s = 481$ Hz (see Section 2.1.4).

4.1.4 Data Analysis

Each revolution of the user around the trajectory was separately analyzed for circularity, enclosed area, and pace. In accordance with [7], x and y end-effector trajectories were
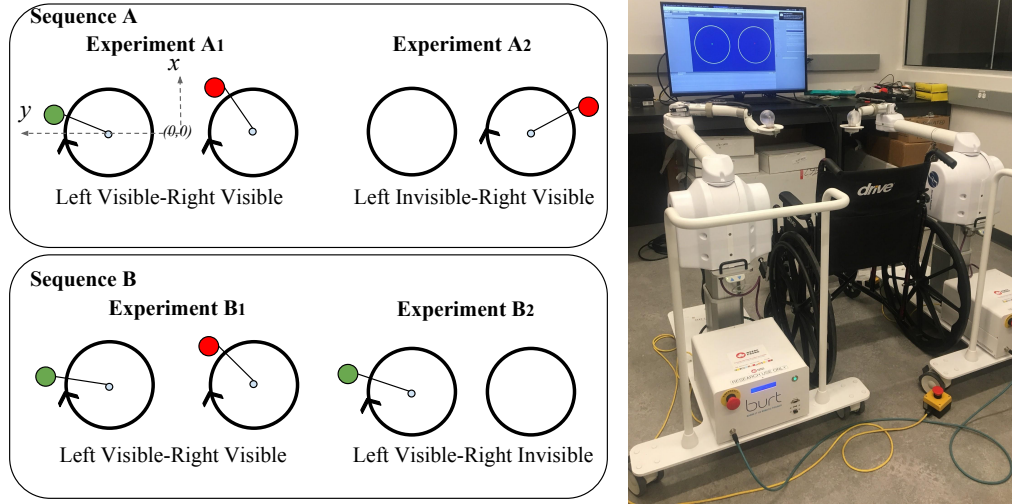
Figure 4.2: Left panel: Subjects perform the experiments either in A-B or B-A order. The visual feedback from dominant and non-dominant hands is withdrawn in experiments B_2 and A_2, respectively. X^+ (vertical) points upward and Y^+ points medial, and the centers of two circles are displayed at a distance equal to 40 cm from each other. The feedback for the right and left hands positions are displayed with red and green solid circles, respectively.

first processed with a 2nd order Butterworth filter with a cutoff frequency of 10 Hz. The sample corresponding to the start of the ith revolution boundary in time series data, i.e. $n_{max,i}$, were identified by detecting peaks in y-position data. All data were processed using MATLAB (R2018b, MathWorks Inc, USA). An ellipse [7] was fitted to the identified boundary to extract circularity and pace measures.

Performance metrics

For the ith revolution, the ellipse fitting algorithm outputs the coordinate of the center, the length of the minor (a_i) and major (b_i) axes. The aforementioned values along with the area of the fitted ellipse, $A_i = \frac{\pi \cdot a_i \cdot b_i}{4}$, were further used as the metrics in our analysis.

For each revolution, the aspect ratio (AR), a measure of circularity [7], was obtained as $AR_i = \frac{a_i}{b_i}$. A perfect circle has an AR equal to 1, while 0 displays a straight line.

The distance-from-center variance (DFCV), i.e. the variance of the distance of all points on the ith unfiltered boundary to the center [7] was used to further quantify the circularity of the motion. Decreasing variance indicates improved circularity.

The duration of each revolution was estimated from the timings of peaks (time elapsing between two successive peaks). The cycling frequency i.e. $\Delta_i = f_s/(n_{max,i} - n_{max,i-1})$, allowing us to have an estimate of the pace for each circle.

Statistical analysis

The comparisons were made between the DH and NDH, and for each hand separately in all transitions, e.g. from A_1 to A_2 and B_1 to B_2. Due to the non-Gaussian distribution of the metrics, non-parametric statistical methods were applied. Trends were investigated (a) within-subject, where one-tailed Wilcoxon rank-sum test (significance level $\alpha = 0.05$) was used to compare left and right revolutions traced by the same subject in each condition, and (b) across subjects, where the means are recomputed for each contrast so as to obtain six pairs, one per subject, and one-tailed Wilcoxon signed-rank test ($\alpha = 0.05$) was applied to these pairs. Cohen's term d is used as an effect size index. The correlation between cycling frequency and circularity is quantified by the coefficient of determination (r^2) of the least-squares linear regression of these metrics, for both AR and DFCV circularity.
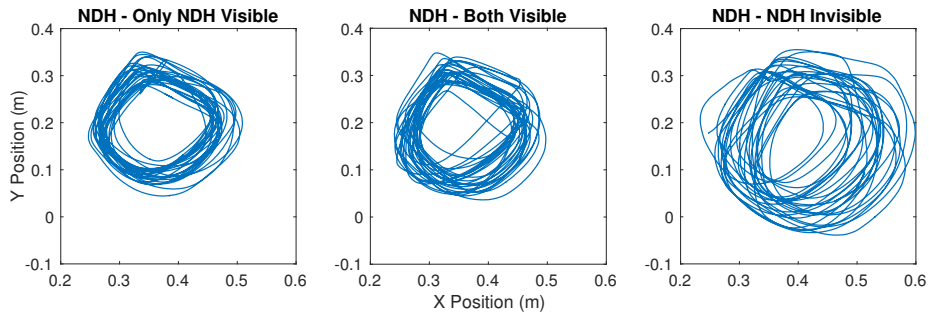
4.2   Results and Discussion

Figure 4.3: Representative trajectories from a single subject's left hand for three experimental conditions: only the left hand receiving feedback, both hands receiving feedback, and the left hand receiving no feedback.

4.2.1 Results

Features were extracted from 685 circles drawn by all subjects during the experiments (340 were traced by NDH, Table 4.1). Fig. 4.3 shows a typical result for the NDH across all experimental conditions. For all but one subject in the DFCV metric, (r^2) of the fitted lines between cyclic frequency and both circularity metrics are less than < 0.1. This indicates a very weak correlation between circle drawing rate and circularity. Similarly, a comparison of cyclic frequency and circularity for all 685 circles showed a linear fit of $r^2 = 0.08$ and $r^2 = 0.03$ for AR and DFCV, respectively.

Dominant versus Non-Dominant Hand

Across-subject analysis over all experimental conditions, showed a higher circularity for DH (AR: 0.791±0.052 and DFCV: 0.24±0.16mm) than NDH (AR: 0.767±0.121 and DFCV: 0.377±0.313 mm), both statistically significant, $p < 0.01$, $d_{AR} = 0.20$, $d_{DFCV} = 0.44$. With the hands in the free visual condition, A_1 and B_1, the DH (DFCV: 0.052±0.017 mm) traced more circular trajectories than the NDH did (DFCV: 0.099±0.050 mm), $p < 0.05$, $d_{DFCV} = 0.94$. In their visually guided modes, the circularity of the right DH trajectories in condition A_2 (DFCV: 0.047±0.013 mm) was significantly higher than the NDH trajectories in condition B_2 (DFCV: 0.122±0.077 mm), $p < 0.05$, $d_{DFCV} = 0.97$.

The within-subject comparison between DH in experiment B_2 and NDH in experiment A_2, hand in invisible mode, showed significant DFCV differences on 3 out of 6 subjects, manifesting in better performance of DH ($p < 0.01$, $d_1 = 0.40$, $d_2 = 0.66$, $d_6 = 1.45$). One subject performed significantly better with the NDH ($p < 0.01$, $d_4 = 1.57$). The same comparison on AR (Table 4.1 and Fig. 4.4) showed 2 subjects had a significantly better performance with their DH ($p < 0.01$, $d_2 = 0.90$, $d_6 = 1.95$), and 2 with their NDH in the invisible mode ($p < 0.01$, $d_4 = 1.89$, $d_5 = 1.71$). There was no statistical difference at the group level when comparing circularity performance of the DH (AR: 0.791±0.052, DFCV: 0.241±0.162 mm) and NDH (AR: 0.767±0.121, DFCV: 0.377±0.317 mm) in the invisible condition (AR: $p = 0.42$, $d_{AR} = 0.20$, DFCV: $p = 0.15$, $d_{DFCV} = 0.43$).

Within-Limb Alterations After Visual Feedback Withdrawal

Transitioning from visible to invisible mode, both DH and NDH in their invisible modes displayed less circularity in terms of AR and DFCV metrics than when they are provided with explicit visual feedback. For instance, blocking the visual information of the left hand

(from experiment A_1 to A_2) significantly decreased the circularity of the left trajectory (DFCV: 0.107±0.062 mm to 0.377±0.313 mm, $p < 0.05$, $d = 0.86$; AR: 0.824±0.054 to 0.767±0.121, $p < 0.05$, $d = 0.47$). Similarly, the circularity of right trajectories decreased significantly after transitioning from experiment B_1 to B_2 (DFCV: 0.049±0.018 mm to 0.241±0.162 mm, $p < 0.01$, $d = 1.04$; AR: 0.882±0.034 to 0.791±0.052, $p < 0.01$, $d = 1.75$). Additionally, there was a significant increase for both hands in the length of the major axes (DH: 0.206±0.011 m to 0.307±0.075 m, $p < 0.05$, $d = 1.35$; NDH: 0.225±0.014 m to 0.321±0.041 m, $p < 0.05$, $d = 2.34$) and minor axes (DH: 0.181±0.010 m to 0.240±0.051 m, $p < 0.05$, $d = 1.18$; NDH: 0.188±0.007 m to 0.245±0.047 m, $p < 0.05$, $d = 1.21$) of the fitted ellipses in absence of visual feedback. Since AR does not change significantly for the NDH between conditions B_1 and B_2, and for the DH between conditions A_1 and A_2, the trajectories maintain approximately the same shape. The area increased significantly for both hands (Fig. 4.5) when visual feedback is removed on either hand (DH: 293±27 cm^2 to 607±295 cm^2, $p < 0.01$, $d = 1.06$; NDH: 332±26 cm^2 to 630±177 cm^2, $p < 0.01$, $d = 1.68$).

Across subjects, for both major and minor axes, significant differences were observed between visually-guided and invisible modes, *i.e.* conditions A_2 and B_2, using a one-tailed signed-rank test for both the DH (major axis: 0.220±0.012 m to 0.307±0.075 m, $p < 0.05$, $d = 1.16$; minor axis: 0.193±0.014 m to 0.240±0.051 m, $p < 0.05$, $d = 0.92$) and the NDH (major axis: 0.321±0.041 m to 0.236±0.020 m, $p < 0.05$, $d = 2.07$; minor axis: 0.245±0.047 m to 0.195±0.009 m, $p < 0.05$, $d = 1.06$). The larger ellipses were drawn in the invisible condition, followed by the visually-guided condition, with the smallest traces drawn in the both-visible condition.

Comparing the mean pace for each subject's NDH hand during both-hands-visible conditions (A_1 and B_1) with one-hand-visible (A_2 and B_2) revealed that subjects followed the desired trajectory more slowly when visual feedback was provided for both hands (0.28±0.12 vs 0.32±0.14 Hz for NDH, $p < 0.001$, $d = 0.33$), as shown in Fig. 4.6. An identical test for right-hand data exhibited similar results (0.27±0.12 vs. 0.32±0.14 Hz, $p < 0.001$, $d = 0.42$).

4.2.2 Discussion

With regards to the relationship between self-reported handedness and circularity, our hypothesis that the DH would trace more circular trajectories than the NDH across all trajectories was observed in only two of the three conditions. In the free-visual and visually-guided modes, the DH trajectories were more circular, however, in the invisible mode, no

Table 4.1: Mean values of both circularity metrics for hands in the invisible mode on a per-subject basis. The number of circles draw in each condition, n, is also shown for each subject in each condition. Statistically significant pairs are indicated by $*$.

Subj.	Aspect Ratio			DFCV (mm)			n ($^{\text{NDH}}/_{\text{DH}}$)			
	NDH-A_2	DH-B_2		NDH-A_2	DH-B_2		A_1	A_2	B_1	B_2
1	0.77 (0.07)	0.79 (0.10)		0.24 (0.13)	0.16 (0.20)	$*$	$^{25}/_{25}$	$^{24}/_{24}$	$^{27}/_{27}$	$^{23}/_{23}$
2	0.80 (0.07)	0.87 (0.07)	$*$	0.11 (0.07)	0.06 (0.05)	$*$	$^{16}/_{16}$	$^{17}/_{18}$	$^{8}/_{8}$	$^{18}/_{17}$
3	0.77 (0.11)	0.81 (0.07)		0.40 (0.37)	0.31 (0.18)		$^{10}/_{11}$	$^{9}/_{9}$	$^{8}/_{8}$	$^{9}/_{9}$
4	0.87 (0.05)	0.74 (0.07)	$*$	0.12 (0.07)	0.52 (0.26)	$*$	$^{4}/_{5}$	$^{5}/_{6}$	$^{5}/_{6}$	$^{7}/_{7}$
5	0.86 (0.05)	0.73 (0.08)	$*$	0.45 (0.54)	0.24 (0.10)		$^{7}/_{8}$	$^{9}/_{9}$	$^{8}/_{8}$	$^{9}/_{9}$
6	0.54 (0.14)	0.81 (0.09)	$*$	0.95 (0.55)	0.15 (0.15)	$*$	$^{23}/_{23}$	$^{32}/_{32}$	$^{16}/_{16}$	$^{21}/_{21}$
Mean	0.77 (0.08)	0.79 (0.08)		0.38 (0.29)	0.24 (0.16)		12.8	14.2	12.1	14.4
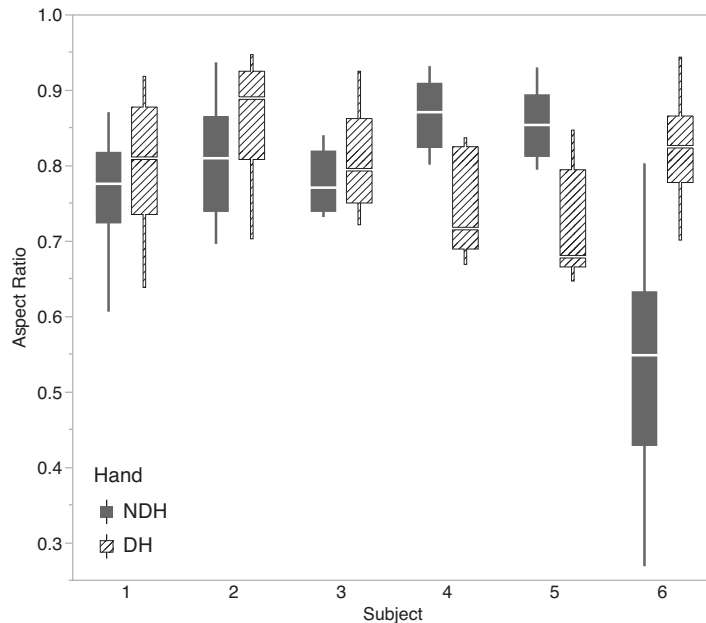
Figure 4.4: Aspect ratio for each subject with hands in their respective invisible conditions. Subjects 2 and 6 show significantly better circularity on their DH, subjects 4 and 5 show significantly better circularity on their NDH, and subjects 1 and 3 have no significant difference.

significant results were found at the group level. While previous results from the literature indicated the DH should show better circularity performance than the NDH, this was only true in two of the six subjects tested. Another two subjects traced more circular

Figure 4.5: Area, in m^2, of DH and NDH trajectories for each condition. In conditions A_2 and B_2, both hands trace significantly different areas compared to the free-visual conditions A_1 and B_1.

trajectories with their NDH, and the final two subjects showed no significant difference in circularity.

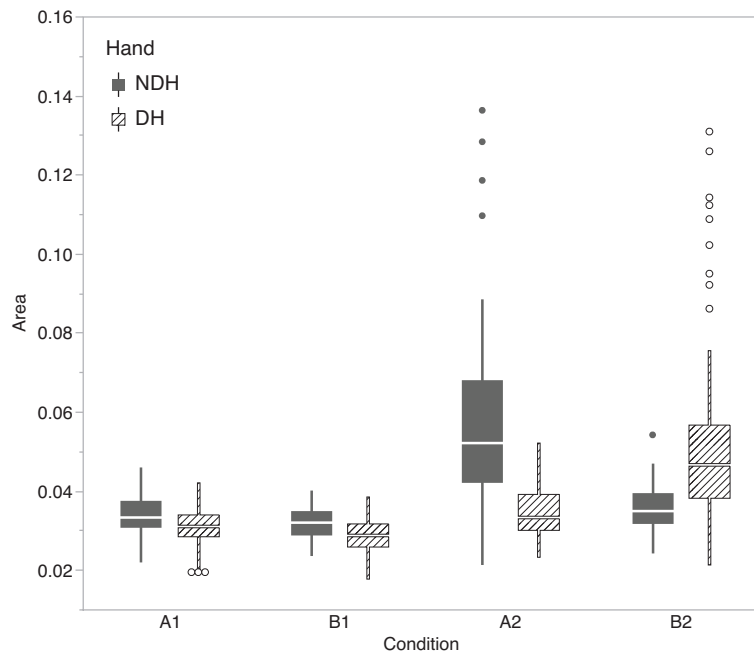One postulation for this observation is that, while the DH is known to act more dexterously in presence of visual feedback than NDH, when visual information was removed subjects relied solely on proprioception and forward models, likely better shaped for the DH in unimanual tasks. Our preliminary results also suggest the possibility of specific forward models for bimanual tasks which are different than the summation of unimanual forward models. Subsequent experiments to systematically explore this hypothesis are warranted.

Based on the effect size seen for the statistically insignificant group level result in the invisible condition, this pilot study reveals the need for at least $N = 42$ subjects, ideally 21 of each handedness, in a future full-scale experiment [47, pp. 302-303]. With the appropriate number of participants, subsequent work would be sufficiently statistically powered $(1 - \beta = 0.8, \alpha = 0.05)$ so as to avoid a type II error and draw more meaningful conclusions about the relationship between handedness and visual feedback during a NMS-BCT.
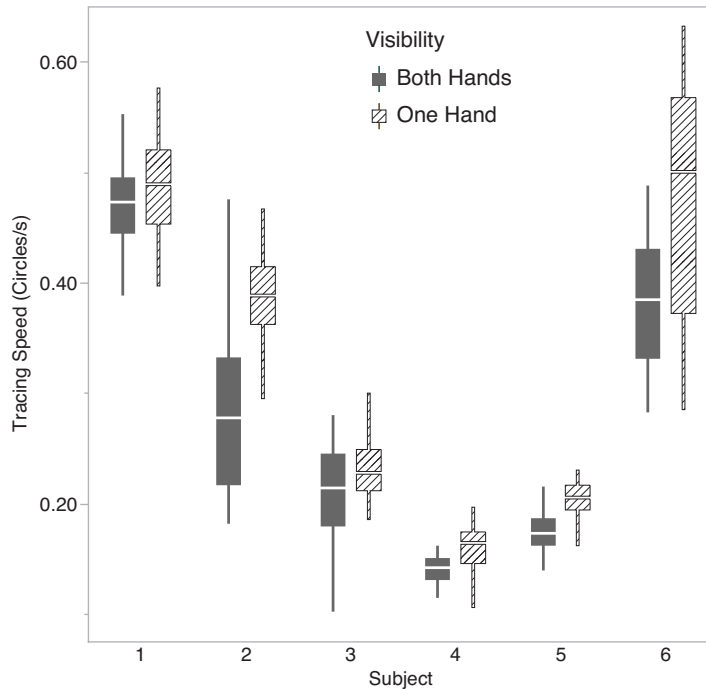
50

Figure 4.6: Tracing Speed by Subject. The difference between the "Both Hands" and "One Hand" visibility conditions is significant ($p < 0.01$) in all but subjects 1 and 3.

In agreement with the second hypothesis, participants traced target trajectories more quickly with feedback from only one hand. Despite increased speed, circularity performance did not vary significantly for a given hand between the free-visual condition and its visually-guided mode (e.g. A_1 to A_2, for the right hand). This suggests that subjects adjusted their speed to maintain a threshold of perceived satisfactory circularity. To stay above this threshold, a decrease in tracing rate was observed during the free-visual condition. Decreased speed may also account for attentional shifts between visual feedback of each hand. Future work will investigate the critical role that attention plays in these experiments.

The areas of the ellipses fit to each revolution of the trajectory vary by the experimental condition. The largest elliptical areas were observed for hands in the invisible condition (with no significant difference between DH and NDH), followed by traces from the visually-guided condition. The smallest areas were traced in the free-visual condition. This is in contrast to the experiment by Swinnen et al. [55] in which subjects performed a MS-BCT. They found that the traced circle diameters were largest for the condition where only the DH was visible, followed by the free-visual condition, with their smallest circles

being traced while the NDH was visible. Also in disagreement with our results, Franz [21] reported that, in a MS-BCT, the "visually attended" hand traces larger circles than the hand obscured. These discrepancies warrant a deeper investigation into the differences between MS and NMS trajectories during a BCT.

4.3   Improvements to Apparatus

During the experiment, there was no attempt to compensate for the robot's dynamics, aside from gravity compensation and the control action constraining the end-effector to the transverse plane, as development of the computed-torque admittance controller was still in progress at the time of the study. The interaction forces felt by the participant varied depending on the configuration of the BURT and, because the task was in-phase and non-mirror symmetric on a bimanual system with mirrored kinematics, the impedance presented to each limb was not congruent. That is, the impedance felt by the left hand passing through the nine o'clock position was not the same as that felt by the right hand at the same time. Peak values of the norm of the interaction force is approximately 20 N for faster tracers. As a result, participants had to first learn a complex set of dynamic behaviours of the BURT system around their desired trajectory before they could effectively perform the task. However, aside from a 60 s familiarization period before collecting data, no statistical improvement was found in the performance of the free-visual condition trials between the start and end of the experiment. This suggests that over the course of a subject's interaction with the BURT, little changed in the participant's compensation for the BURT's dynamics. The distinct teardrop shape of the trajectories in Fig. 4.3 makes it apparent that the impedance was not constant in all directions across the workspace.

In future experiments, an impedance or admittance controller could be used to produce a uniform impedance for the participant to interact with. These intuitive dynamics would ideally be as high admittance as possible to generate smaller interaction forces to overcome along the trajectory. As discussed in Section 1.1.2, an impedance controller may be ineffective at masking the inherent inertia of the manipulator and the stability of admittance controller is less likely when rendering low-impedance dynamics. This suggests a certain maximum admittance that the device could render while ensuring participant safety. The selection of this value should balance the desire for a haptically transparent system, to prevent operator fatigue and participants modifying their behaviour in response to large interaction force, with the requirement of uniform and intuitive dynamic behaviour.

Chapter 5

Conclusion and Recommendations

5.1 Conclusion

This thesis explored the estimation of physical human-robot interaction dynamics through two applications of the BURT robotic platform.

First, a novel testbed for validating the performance of realtime operator impedance estimators was designed. The pHRI is simulated by rigidly connecting the end-effectors of each arm of the BURT system, allowing one robot to present a time-varying, known impedance to the other. An admittance control law is implemented to mask the natural dynamics of BURT, and its performance is verified experimentally. Consideration is also given to the design of the coupling and the exciting trajectories. Trials of this robot-robot interaction using a suite of least-squares estimators from the literature demonstrate its efficacy and utility.

Secondly, the BURT was used as a research platform in a human sensorimotor experiment. While participants were engaged in a non-mirror-symmetric bimanual circle-drawing task, visual feedback of the task performance was withdrawn from one of the hands. Relationships between the visibility, circularity, tracing speed, and subject handedness are examined. The results showed that there was not a strong relationship between handedness and circularity performance without visual feedback. For example, right handed subjects are in general no better at maintaining the trajectory with their right hand in the absence of visual feedback than with their left. It was also found that tracing speed increased when visual feedback was only provided for a single hand.

5.2 Recommendations

The control of the testbed could be made more robust by improving the estimate of velocity. Currently, phase lag in the velocity estimate from low-pass filtering leads to instabilities for higher derivative gains when a PD position control law is used. The use of external sensors or better position signal processing would allow the testbed to render a wider range of admittances with higher fidelity.

Future investigation into task-specific operator impedance estimators that leverage results from human motor control research are recommended. During point-to-point movements, for example, the human is known to obey the minimum jerk criteria, which allows an estimator to predict the desired trajectory and improve estimation accuracy. For a particular task, a cost function (such as minimum jerk) can be identified by solving the IOC problem. As the understanding of human neuromechanics grows, controllers and estimators designed for pHRI must incorporate results from the field to achieve their best performance.

During the human motor control experiment presented in Chapter 4, the dynamics of the robot were not uniform throughout the workspace. For example, at locations on the target trajectory where the desired task-space motions came largely from one of the BURT's shoulder joints, the participant felt a relatively large inertia; when the motion arose from the elbow joint, the perceived inertia was much smaller. It is recommended that the BURT be admittance-controlled during future studies to provide that is free of the manipulator's parasitic dynamics This will reduce operator fatigue and eliminate the confound of large, non-intuitive manipulator impedance.

A more rigorous study of the relationship between circularity performance, handedness, and attention is warranted. It is recommended that future experiments in this vein better guide the attention of participants by using a fixation cross. A more in depth study of the role of attention may also employ head or eye-tracking technology to glean insight into the nature of attention during the BCT task, especially as it relates to handedness.

References

[1] *BURT D-H frames*. Barrett Technology LLC, May 2018.

[2] *BURT System Overview*. Barrett Technology LLC, May 2018.

[3] R. J. Adams and B. Hannaford. Stable haptic interaction with virtual environments. *IEEE Transactions on Robotics and Automation*, 15(3):465–474, June 1999.

[4] Fausto Baldissera, Paolo Cavallari, and Pietro Civaschi. Preferential coupling between voluntary movements of ipsilateral limbs. *Neuroscience letters*, 34(1):95–100, 1982.

[5] Etienne Burdet, Rieko Osu, David W. Franklin, Theodore E. Milner, and Mitsuo Kawato. The central nervous system stabilizes unstable dynamics by learning optimal impedance. *Nature*, 414:446–449, 2001.

[6] Winston D Byblow, Jeffery J Summers, Andras Semjen, Irina J Wuyts, and Richard G Carson. Spontaneous and intentional pattern switching in a multisegmental bimanual coordination task. *Motor Control*, 3(4):372–393, 1999.

[7] Richard G Carson, Julie Thomas, Jeffery J Summers, Megan R Walters, and Andras Semjen. The dynamics of bimanual circle drawing. *The Quarterly Journal of Experimental Psychology Section A*, 50(3):664–683, 1997.

[8] X. Chen, C. Yang, C. Fang, and Z. Li. Impedance matching strategy for physical human robot interaction control. In *2017 13th IEEE Conference on Automation Science and Engineering (CASE)*, pages 138–144, Aug 2017.

[9] E. Colgate and N. Hogan. An analysis of contact instability in terms of passive physical equivalents. In *Proceedings, 1989 International Conference on Robotics and Automation*, pages 404–409 vol.1, May 1989.

[10] J. E. Colgate and J. M. Brown. Factors affecting the z-width of a haptic display. In *Proceedings of the 1994 IEEE International Conference on Robotics and Automation*, pages 3205–3210 vol.4, May 1994.

[11] J. E. COLGATE and N. HOGAN. Robust control of dynamically interacting systems. *International Journal of Control*, 48(1):65–88, 1988.

[12] J. E. Colgate and G. Schenkel. Passivity of a class of sampled-data systems: application to haptic interfaces. In *Proceedings of 1994 American Control Conference - ACC '94*, volume 3, pages 3236–3240 vol.3, June 1994.

[13] Simone Cardoso de Oliveira and Sébastien Barthélémy. Visual feedback reduces bimanual coupling of movement amplitudes, but not of directions. *Experimental Brain Research*, 162(1):78–88, 2005.

[14] F. Dimeas and N. Aspragathos. Online stability in human-robot cooperation with admittance control. *IEEE Transactions on Haptics*, 9(2):267–278, April 2016.

[15] N. Diolaiti, C. Melchiorri, and S. Stramigioli. Contact impedance estimation for robotic systems. *IEEE Transactions on Robotics*, 21(5):925–935, Oct 2005.

[16] V. Duchaine and C. Gosselin. Safe, stable and intuitive control for physical human-robot interaction. In *2009 IEEE International Conference on Robotics and Automation*, pages 3383–3388, May 2009.

[17] V. Duchaine and C. M. Gosselin. Investigation of human-robot interaction stability using lyapunov theory. In *2008 IEEE International Conference on Robotics and Automation*, pages 2189–2194, May 2008.

[18] F. Ficuciello, A. Romano, L. Villani, and B. Siciliano. Cartesian impedance control of redundant manipulators for human-robot co-manipulation. In *2014 IEEE/RSJ International Conference on Intelligent Robots and Systems*, pages 2120–2125, Sep. 2014.

[19] T Flash and N Hogan. The coordination of arm movements: an experimentally confirmed mathematical model. *Journal of Neuroscience*, 5(7):1688–1703, 1985.

[20] Michele Focchi, Gustavo A. Medrano-Cerda, Thiago Boaventura, Marco Frigerio, Claudio Semini, Jonas Buchli, and Darwin G. Caldwell. Robot impedance control and passivity analysis with inner torque and velocity feedback loops. *Control Theory and Technology*, 14(2):97–112, May 2016.

[21] Elizabeth A Franz. Attentional distribution of task parameters to the two hands during bimanual performance of right-and left-handers. *Journal of Motor Behavior*, 36(1):71–81, 2004.

[22] W. Gallagher and J. Ueda. A haptic human-robot interface accounting for human parameter stochasticity. In *2014 IEEE International Conference on Robotics and Automation (ICRA)*, pages 4256–4261, May 2014.

[23] William Gallagher, Dalong Gao, and Jun Ueda. Improved stability of haptic humanrobot interfaces using measurement of human arm stiffness. *Advanced Robotics*, 28(13):869–882, 2014.

[24] J. J. Gil, E. Sanchez, T. Hulin, C. Preusche, and G. Hirzinger. Stability boundary for haptic rendering: Influence of damping and delay. In *Proceedings 2007 IEEE International Conference on Robotics and Automation*, pages 124–129, April 2007.

[25] H. Hatze. A myocybernetic control model of skeletal muscle. *Biological Cybernetics*, 25(2):103–119, Jun 1977.

[26] Herbert Hatze. A complete set of control equations for the human musculo-skeletal system. *Journal of Biomechanics*, 10(11):799 – 805, 1977.

[27] M. D. Hill and G. Niemeyer. Real-time estimation of human impedance for haptic interfaces. In *World Haptics 2009 - Third Joint EuroHaptics conference and Symposium on Haptic Interfaces for Virtual Environment and Teleoperator Systems*, pages 440–445, March 2009.

[28] N. Hogan. Adaptive control of mechanical impedance by coactivation of antagonist muscles. *IEEE Transactions on Automatic Control*, 29(8):681–690, August 1984.

[29] Neville Hogan. Impedance control: An approach to manipulation: Part itheory. *Journal of Dynamic Systems, Measurement, and Control*, 107, 1985.

[30] T. Hulin, C. Preusche, and G. Hirzinger. Stability boundary for haptic rendering: Influence of human operator. In *2008 IEEE/RSJ International Conference on Intelligent Robots and Systems*, pages 3483–3488, Sep. 2008.

[31] Hiroshi Imamizu and Shinsuke Shimojo. The locus of visual-motor learning at the task or manipulator level: implications from intermanual transfer. *Journal of Experimental Psychology: Human Perception and Performance*, 21(4):719, 1995.

[32] K.C. Nishikawa J.A. Monroy, A.K. Lappin.

[33] S. H. Kang, M. Jin, and P. Hun Chang. A solution to the accuracy/robustness dilemma in impedance control. *IEEE/ASME Transactions on Mechatronics*, 14(3):282–294, June 2009.

[34] H. Kazerooni and P. M. Bobgan. Human induced instability in powered hand controllers. In *Proceedings 1992 IEEE International Conference on Robotics and Automation*, pages 755–760 vol.1, May 1992.

[35] R. E. Kearney, R. B. Stein, and L. Parameswaran. Identification of intrinsic and reflex contributions to human ankle stiffness dynamics. *IEEE Transactions on Biomedical Engineering*, 44(6):493–504, June 1997.

[36] Arvid QL Keemink, Herman van der Kooij, and Arno HA Stienen. Admittance control for physical humanrobot interaction. *The International Journal of Robotics Research*, 37(11):1421–1444, 2018.

[37] D. A. Lawrence. Stability and transparency in bilateral teleoperation. *IEEE Transactions on Robotics and Automation*, 9(5):624–637, Oct 1993.

[38] Perry Li, Roberto Horowitz, and Ieee Asme. Control of smart exercise machines. part ii: Self-optimizing control. 09 1997.

[39] L. J. Love and W. J. Book. Environment estimation for enhanced impedance control. In *Proceedings of 1995 IEEE International Conference on Robotics and Automation*, volume 2, pages 1854–1859 vol.2, May 1995.

[40] Lonnie Joe Love. *Adaptive Impedance Control*. PhD thesis, Atlanta, GA, USA, 1995. UMI Order No. GAX96-06167.

[41] R. G. Marteniuk, C. L. MacKenzie, and D. M. Baba. Bimanual movement control: Information processing and interaction effects. *The Quarterly Journal of Experimental Psychology Section A*, 36(2):335–365, 1984.

[42] Katja D. Mombaur, Anh Truong, and Jean-Paul Laumond. From human to humanoid locomotionan inverse optimal control approach. *Autonomous Robots*, 28:369–383, 2010.

[43] Mina Nouredanesh, Matthew Frazer, James Tung, Soo Jeon, and Arash Arami. Effect of visual information on dominant and non-dominant hands during bimanual drawing

with a robotic platform. In *2019 IEEE 16th International Conference on Rehabilitation Robotics (ICORR)*, pages 1221–1226. IEEE, 2019.

[44] C. Ott, R. Mukherjee, and Y. Nakamura. Unified impedance and admittance control. In *2010 IEEE International Conference on Robotics and Automation*, pages 554–561, May 2010.

[45] M. C. Priess, R. Conway, J. Choi, J. M. Popovich, and C. Radcliffe. Solutions to the inverse lqr problem with application to biological systems analysis. *IEEE Transactions on Control Systems Technology*, 23(2):770–777, March 2015.

[46] M. M. Rahman, R. Ikeura, and K. Mizutani. Investigating the impedance characteristic of human arm for development of robots to co-operate with human operators. In *IEEE SMC'99 Conference Proceedings. 1999 IEEE International Conference on Systems, Man, and Cybernetics (Cat. No.99CH37028)*, volume 2, pages 676–681 vol.2, Oct 1999.

[47] Bernard Rosner. *Fundamentals of Biostatistics*. Brooks/Cole, 7 edition, 2011.

[48] Abraham. Savitzky and M. J. E. Golay. Smoothing and differentiation of data by simplified least squares procedures. *Analytical Chemistry*, 36(8):1627–1639, 1964.

[49] Bruno Siciliano and Oussama Khatib. *Springer Handbook of Robotics*. Springer-Verlag, Berlin, Heidelberg, 2007.

[50] S. K. Singh and D. O. Popa. An analysis of some fundamental problems in adaptive control of force and impedance behavior: theory and experiments. *IEEE Transactions on Robotics and Automation*, 11(6):912–921, Dec 1995.

[51] Thomas Sinkjr and Ryoichi Hayashi. Regulation of wrist stiffness by the stretch reflex. *Journal of Biomechanics*, 22(11):1133 – 1140, 1989.

[52] Jean-Jacques E. Slotine and Weiping Li. *Applied nonlinear control*. Prentice-Hall, 1991.

[53] Rebecca MC Spencer, Richard B Ivry, Daniel Cattaert, and Andras Semjen. Bimanual coordination during rhythmic movements in the absence of somatosensory feedback. *Journal of Neurophysiology*, 94(4):2901–2910, 2005.

[54] M.W. Spong, S. Hutchinson, and M. Vidyasagar. *Robot Modeling and Control*. Wiley, 2005.

[55] Stephan P Swinnen, Kris Jardin, and Ruud Meulenbroek. Between-limb asynchronies during bimanual coordination: effects of manual dominance and attentional cueing. *Neuropsychologia*, 34(12):1203–1213, 1996.

[56] T. Tsuji, K. Ito, and H. Nagaoka. Identification and regulation of mechanical impedance for force control of robot manipulators. *IFAC Proceedings Volumes*, 23(8, Part 5):169 – 174, 1990. 11th IFAC World Congress on Automatic Control, Tallinn, 1990 - Volume 5, Tallinn, Finland.

[57] T. Tsumugiwa, R. Yokogawa, and K. Yoshida. Stability analysis for impedance control of robot for human-robot cooperative task system. In *2004 IEEE/RSJ International Conference on Intelligent Robots and Systems (IROS) (IEEE Cat. No.04CH37566)*, volume 4, pages 3883–3888 vol.4, Sep. 2004.

[58] Tomer Valency and Miriam Zacksenhouse. Accuracy/Robustness Dilemma in Impedance Control . *Journal of Dynamic Systems, Measurement, and Control*, 125(3):310–319, 09 2003.

[59] M. Vidyasagar. *Nonlinear Systems Analysis (2Nd Ed.)*. Prentice-Hall, Inc., Upper Saddle River, NJ, USA, 1992.

[60] Z. Wang, A. Peer, and M. Buss. Fast online impedance estimation for robot control. In *2009 IEEE International Conference on Mechatronics*, pages 1–6, April 2009.

[61] F.E. Zajac. Muscle and tendon: Properties, models, scaling, and application to biomechanics and motor control. *Critical reviews in biomedical engineering*, 17:359–411, 02 1989.